A new perspective for nonadiabatic dynamics with phase space mapping models

Xin He (iD), and Jian Liu (iD)

COLLECTIONS

Paper published as part of the special topic on Chemical Physics of Supercooled Water

View Online   Export Citation   CrossMark

ARTICLES YOU MAY BE INTERESTED IN

A new perspective for nonadiabatic dynamics with phase space mapping models

View Online   Export Citation   CrossMark

Xin He (ID) and Jian Liu[a] (ID)

AFFILIATIONS

Beijing National Laboratory for Molecular Sciences, Institute of Theoretical and Computational Chemistry,
College of Chemistry and Molecular Engineering, Peking University, Beijing 100871, China

Note: This paper is part of a JCP Special Topic on Dynamics of Open Quantum Systems.
[a]**Electronic mail:** jianliupku@pku.edu.cn

ABSTRACT

Based on the recently developed unified theoretical framework [J. Liu, J. Chem. Phys. **145**(20), 204105 (2016)], we propose a new perspective for studying nonadiabatic dynamics with classical mapping models (CMMs) of the coupled multistate Hamiltonian onto the Cartesian phase space. CMMs treat the underlying electronic state degrees of freedom classically with a simple physical population constraint while employing the linearized semiclassical initial value representation to describe the nuclear degrees of freedom. We have tested various benchmark condensed phase models where numerically exact results are available, which range from finite temperature to more challenging zero temperature, from adiabatic to nonadiabatic domains, and from weak to strong system-bath coupling regions. CMMs demonstrate overall reasonably accurate dynamics behaviors in comparison to exact results even in the asymptotic long time limit for various spin-boson models and site-exciton models. Further investigation of the strategy used in CMMs may lead to practically useful approaches to study nonadiabatic processes in realistic molecular systems in the condensed phase.

Published under license by AIP Publishing. https://doi.org/10.1063/1.5108736

I. INTRODUCTION

There is considerable effort focused on developing practical trajectory-based dynamics approaches for describing nonadiabatic processes in complex (molecular) systems in chemistry, biology, and materials science.[1–73] Most of these trajectory-based approaches can be included in several categories, such as mean field trajectory (MFT) method (Ehrenfest dynamics),[2–7] surface hopping,[8–24] mixed quantum-classical dynamics,[28–32] mixed quantum-classical path integral,[25–27] multiple spawning/cloning,[34–38] and Meyer-Miller mapping Hamiltonian model.[39–49,51–61,63] The last category is based on Meyer and Miller's pioneering work in which a multi-electronic-state (MES) Hamiltonian operator was mapped onto continuous degrees of freedom (DOFs).[39] Stock and Thoss have proved that the Meyer-Miller mapping Hamiltonian is, in principle, exact in quantum mechanics.[55] The Meyer-Miller mapping model has offered a theoretical framework to develop useful nonadiabatic dynamics and thermodynamics methods.[40–49,51,55–63,74–76] The two important elements often used in the literature of the Meyer-Miller mapping model[39–49,51–59,62,74] are the following:

(1) The underlying electronic state degrees of freedom (DOFs) should be quantized and then treated semiclassically or quasiclassically for nonadiabatic dynamics to go beyond the conventional Ehrenfest dynamics/mean field trajectory method.

(2) A space of singly excited oscillators (SEOs) should be employed to construct and apply the Meyer-Miller mapping model based on Schwinger's formulation,[77,78] which has been evident from the work by Stock and Thoss[55] in 1997 as well as that by Sun, Wang, and Miller[40] in 1998.

We have recently proposed a novel unified framework to construct approaches for the mapping of the multistate Hamiltonian operator onto the Cartesian phase space. The framework provides a new way to derive the famous Meyer-Miller model, and more importantly, it can lead to other exact mapping Hamiltonian models in the Cartesian phase space. Since the unified framework does not invoke a space of SEOs in deriving the phase space mapping models, it presents a new heuristic viewpoint to consider the dynamics of the coupled multistate Hamiltonian. The purpose of this paper is to employ the unified framework[79] to study nonadiabatic dynamics.

This paper is organized as follows. Section II first reviews the theory of the unified framework for phase space mapping models for the multistate Hamiltonian operator and then extends it to deal with nonadiabatic dynamics where both electronic and nuclear DOFs are coupled. Section III presents numerical results of various benchmark model tests for condensed phase systems. Finally, conclusions are given in Sec. IV.

II. THEORY

A. Mapping models in a unified theoretical framework

Consider a Hamiltonian operator for F orthonormal states,

$$\hat{H} = \sum_{m,n=1}^{F} H_{nm}|n\rangle\langle m|. \tag{1}$$

The Hamiltonian matrix is often a real symmetric one, where $H_{nm} = H_{mn}$. (For convenience, the reduced Planck constant is set to $\hbar = 1$ throughout this paper.) We have recently proposed a new unified theoretical framework to construct equivalent representations of the multistate Hamiltonian operator and to present several approaches for the mapping onto the Cartesian phase space.[79,80] The three key elements in the framework are the following:

1) Extend Schwinger's formulation[77,78] to map the F-dimensional Hamiltonian operator onto an $F + 1$ dimensional space. That is, state $|n\rangle$ can be mapped as

$$|n\rangle \mapsto |\underbrace{0_1 \cdots 1_n \cdots 0_F}_{F\text{-states}}\rangle \tag{2}$$

such that it is viewed as a single excitation from the vacuum state $|\bar{0}\rangle \mapsto |\underbrace{0_1 \cdots 0_n \cdots 0_F}_{F\text{-states}}\rangle$, i.e.,

$$|n\rangle = \hat{a}_n^+|\bar{0}\rangle. \tag{3}$$

Here, an excitation represents the occupation of the corresponding state. The vacuum state $|\bar{0}\rangle$ is orthogonal to any occupied state $|n\rangle$.

2) Define creation and annihilation operators such that the $F + 1$ dimensional space is complete for all (combined) excitations. That is,

$$\begin{aligned}\hat{a}_n^+ &= |n\rangle\langle\bar{0}|, \\ \hat{a}_n &= |\bar{0}\rangle\langle n|.\end{aligned} \tag{4}$$

Commutation and anticommutation relations are then naturally constructed.[79]

The multistate Hamiltonian operator of Eq. (1) becomes

$$\hat{H} = \sum_{m,n=1}^{F} H_{nm}\hat{a}_n^+\hat{a}_m \tag{5}$$

with no ambiguity. One also obtains the following relation:

$$\begin{aligned}\hat{\sigma}_x^{(n)} &= \hat{a}_n + \hat{a}_n^+, \\ \hat{\sigma}_y^{(n)} &= \frac{\hat{a}_n - \hat{a}_n^+}{i},\end{aligned} \tag{6}$$

where $\hat{\sigma}_x^{(n)}$ and $\hat{\sigma}_y^{(n)}$ are two Pauli operators (for a spin 1/2 particle).

3) Derive equivalent representations of the Hamiltonian operator (in terms of $\left\{\hat{\sigma}_x^{(n)}, \hat{\sigma}_y^{(n)}\right\}$) and propose the criteria for mapping them onto the Cartesian phase space such that classical/quasiclassical/semiclassical/quantum dynamics can be employed.[79]

The new framework employs *only* quantum operators to construct the mapping models, without invoking a space of singly excited oscillators (SEOs) as conventionally used in the literature on the Meyer-Miller mapping model.[40,55] (See Appendix A of Ref. 79 for more discussion.) The unified framework offers a novel way[80] to derive the seminal Meyer-Miller mapping model other than the original ones proposed by Meyer and Miller[39] and by Stock and Thoss.[55] It has been shown in Ref. 79 that the *general* semiclassical Meyer-Miller mapping Hamiltonian[80] is

$$H = \sum_{n,m=1}^{F} \frac{1}{2}\left(x^{(n)}x^{(m)} + p^{(n)}p^{(m)} - \gamma_{nm}\right)H_{nm}, \tag{7}$$

where $\gamma_{nn}/2$ is set to $1/2$ in Meyer and Miller's original version[39,55] or chosen to be $\left(\sqrt{3}-1\right)/2$ or other optimal values in its semiclassical/quasiclassical applications,[42,46,53,56,59,81] while $\gamma_{nm}/2$ ($n \neq m$) is often set to 0. Equation (7) is a more compact version of Eq. (43) of Ref. 79. The classical Meyer-Miller mapping Hamiltonian is

$$H = \sum_{n,m=1}^{F} \frac{1}{2}\left(x^{(n)}x^{(m)} + p^{(n)}p^{(m)}\right)H_{nm}, \tag{8}$$

while the quantum version is

$$\hat{H} = \sum_{n,m=1}^{F} \frac{1}{2}\left(\hat{x}^{(n)}\hat{x}^{(m)} + \hat{p}^{(n)}\hat{p}^{(m)} - \hat{\mathbf{1}}\delta_{nm}\right)\hat{H}_{nm}, \tag{9}$$

where $\hat{\mathbf{1}}$ is an identity operator. The Meyer-Miller model involves $2F$ phase space mapping variables for the F electronic DOFs.

Similarly, other phase space mapping models can also be developed from the equivalent representations of the Hamiltonian operator.[79] Another classical mapping model (CMM) for the multistate Hamiltonian operator [Eq. (1) or (5)] is

$$H = \sum_{n,m=1}^{F} H_{nm}\left(x^{(n)}p_y^{(m)} - y^{(n)}p_x^{(m)}\right), \tag{10}$$

which is derived from an analogy to the spin angular momentum in Ref. 79. The mapping Hamiltonian of Eq. (10) for the multistate Hamiltonian operator happens to be identical to the mapping model earlier proposed for the second-quantized many-electron Hamiltonian by Li and Miller.[82] The relation between them can be established by the isomorphism between the multistate Hamiltonian and the second-quantized many-electron Hamiltonian with only 1-electron interactions.[80] We denote Eq. (10) the Li-Miller mapping model (or spin angular momentum mapping model). It employs $4F$ phase space mapping variables for the F electronic DOFs. As demonstrated in Fig. 5 of Ref. 79, the Li-Miller mapping model can outperform the Meyer-Miller mapping model in some regions.

Four more classical mapping models for the multistate Hamiltonian operator (proposed in Ref. 79) are

$$H = \sum_{n=1}^{F} \frac{\left(x^{(n)}+p_y^{(n)}\right)^2 + \left(y^{(n)}-p_x^{(n)}\right)^2}{4} H_{nn}$$
$$+ \sum_{n \neq m} \left(x^{(n)}p_y^{(m)} - y^{(m)}p_x^{(n)}\right)H_{nm}, \tag{11}$$

$$H = \sum_{n=1}^{F} \frac{\left(x^{(n)}+p_y^{(n)}\right)^2 + \left(y^{(n)}-p_x^{(n)}\right)^2}{4} H_{nn}$$
$$+ \sum_{n < m} \left(\left(x^{(n)}x^{(m)} + p_x^{(n)}p_x^{(m)}\right)\right.$$
$$\left. + \left(y^{(n)}y^{(m)} + p_y^{(n)}p_y^{(m)}\right)\right)H_{nm}, \tag{12}$$

$$H = \sum_{n=1}^{F} \frac{\left(x^{(n)}+p_y^{(n)}\right)^2 + \left(y^{(n)}-p_x^{(n)}\right)^2}{4} H_{nn} + \sum_{n < m} \frac{\left(x^{(n)}+p_y^{(n)}\right)\left(x^{(m)}+p_y^{(m)}\right) + \left(y^{(n)}-p_x^{(n)}\right)\left(y^{(m)}-p_x^{(m)}\right)}{2} H_{nm}, \tag{13}$$

and

$$H = \sum_{n=1}^{F} H_{nn}\left(x^{(n)}p_y^{(n)} - y^{(n)}p_x^{(n)}\right)$$
$$+ \sum_{n < m} \left(\left(x^{(n)}x^{(m)} + p_x^{(n)}p_x^{(m)}\right) + \left(y^{(n)}y^{(m)} + p_y^{(n)}p_y^{(m)}\right)\right)H_{nm}. \tag{14}$$

Define P_n as the population of the nth state. Conservation of the total population is

$$\sum_{n=1}^{F} P_n = \sum_{n=1}^{F} \frac{1}{2}\left(x^{(n)}x^{(n)} + p^{(n)}p^{(n)}\right) = 1 \tag{15}$$

for Eq. (8),

$$\sum_{n=1}^{F} P_n = \sum_{n=1}^{F} \left(x^{(n)}p_y^{(n)} - y^{(n)}p_x^{(n)}\right) = 1 \tag{16}$$

for Eq. (10) or (14), or

$$\sum_{n=1}^{F} P_n = \sum_{n=1}^{F} \frac{\left(x^{(n)}+p_y^{(n)}\right)^2 + \left(y^{(n)}-p_x^{(n)}\right)^2}{4} = 1 \tag{17}$$

for Eq. (11), (12), or (13). The five mapping Hamiltonian models [Eqs. (10)–(14)] in the unified framework, which have $4F$ phase space mapping variables for the electronic DOFs, can be related to the Clifford algebra.

It is straightforward to obtain the quantum or semiclassical counterpart for each of these classical mapping models [Eqs. (10)–(14)], similar to the one derived for the Meyer-Miller mapping model by the strategy in the unified framework.[79,80] For instance, the quantum version of the Li-Miller mapping model reads

$$\hat{H} = \sum_{n,m=1}^{F} \left(\hat{x}^{(n)}\hat{p}_y^{(m)} - \hat{y}^{(n)}\hat{p}_x^{(m)} - \frac{1}{2}\hat{\mathbf{1}}\delta_{nm}\right)\hat{H}_{nm}. \tag{18}$$

The semiclassical version takes the form

$$H = \sum_{n,m=1}^{F} H_{nm}\left(x^{(n)}p_y^{(m)} - y^{(n)}p_x^{(m)} - \tilde{\gamma}_{nm}\right), \tag{19}$$

where $\tilde{\gamma}_{nm}$ is a parameter accounting for the quantum commutation.[79,80,82,83] $\tilde{\gamma}_{nm}$ can be set to $1/2\left(\sqrt{3}-1\right)/2$, $1/3$, or other optimal values, while $\tilde{\gamma}_{nm}(n \neq m)$ is often set to 0.

B. Nonadiabatic dynamics with classical mapping models

When the multistate Hamiltonian of Eq. (1) is employed for a coupled multi-electronic-state system, it becomes

$$\hat{H} = \sum_{m,n=1}^{F} H_{nm}\left(\hat{\mathbf{R}},\hat{\mathbf{P}}\right)|n\rangle\langle m| \tag{20}$$

or equivalently

$$\hat{H} = \sum_{m,n=1}^{F} H_{nm}\left(\hat{\mathbf{R}},\hat{\mathbf{P}}\right)\hat{a}_n^{+}\hat{a}_m, \tag{21}$$

where $\hat{\mathbf{R}}$ and $\hat{\mathbf{P}}$ are the coordinate and momentum operators of the nuclear DOFs, respectively.

If one employs the classical Li-Miller mapping Hamiltonian Eq. (10) for the electronic DOFs in Eq. (21), one obtains

$$\hat{H}_{LM} = \sum_{n,m=1}^{F} \left(x^{(n)}p_y^{(m)} - y^{(n)}p_x^{(m)}\right)H_{nm}\left(\hat{\mathbf{R}},\hat{\mathbf{P}}\right). \tag{22}$$

When the diabatic representation of electronic states is used, Eq. (22) becomes

$$\hat{H}_{LM} = \frac{1}{2}\hat{\mathbf{P}}^T\mathbf{M}^{-1}\hat{\mathbf{P}} + \sum_{m,n=1}^{F} \left(x^{(n)}p_y^{(m)} - y^{(n)}p_x^{(m)}\right)V_{nm}\left(\hat{\mathbf{R}}\right). \tag{23}$$

The conservation of the total population Eq. (16) is implicitly used for the kinetic energy term in Eq. (23). (This is a new observation that is essentially the key point of this paper.) The classical Hamiltonian for both nuclear and electronic DOFs is then

$$H_{LM}\left(\mathbf{R},\mathbf{P};\mathbf{x},\mathbf{p_x},\mathbf{y},\mathbf{p_y}\right)$$
$$= \frac{1}{2}\mathbf{P}^T\mathbf{M}^{-1}\mathbf{P} + \sum_{n,m=1}^{F} \left(x^{(n)}p_y^{(m)} - y^{(n)}p_x^{(m)}\right)V_{nm}(\mathbf{R}), \tag{24}$$

where $\mathbf{x}$, $\mathbf{p_x}$, $\mathbf{y}$, and $\mathbf{p_y}$ are the vectors for $\{x^{(n)}\}$, $\left\{p_x^{(n)}\right\}$, $\{y^{(n)}\}$, and $\left\{p_y^{(n)}\right\}$, respectively.

Because the unified framework does not employ SEO states at all but use quantum operators for mapping the multistate Hamiltonian operator onto the Cartesian space, it is natural to do the same to map any physical operators (related to the electronic state DOFs) onto the Cartesian space to study nonadiabatic dynamics where electronic and nuclear DOFs are coupled. For instance, consider the transition probability from state $|n\rangle$ to state $|m\rangle$,

$$\mathrm{Tr}\Big[\hat{\rho}_{nuc}|n\rangle\langle n|e^{i\hat{H}t/\hbar}|m\rangle\langle m|e^{-i\hat{H}t/\hbar}\Big], \quad (25)$$

where $\hat{\rho}_{nuc}$ is the initial density operator for the nuclear DOFs. Equation (25) can be expressed as

$$\mathrm{Tr}\Big[\hat{\rho}_{nuc}\hat{a}_n^+\hat{a}_n\exp\Big(\frac{it}{\hbar}\Big(\sum_{m,n=1}^F H_{nm}(\hat{\mathbf{R}},\hat{\mathbf{P}})\hat{a}_n^+\hat{a}_m\Big)\Big)\hat{a}_m^+\hat{a}_m$$
$$\times \exp\Big(-\frac{it}{\hbar}\Big(\sum_{m,n=1}^F H_{nm}(\hat{\mathbf{R}},\hat{\mathbf{P}})\hat{a}_n^+\hat{a}_m\Big)\Big)\Big]. \quad (26)$$

Note that the trace in Eq. (25) or (26) is over both the electronic state DOFs and nuclear DOFs.

If the classical Li-Miller mapping Hamiltonian Eq. (10) for the electronic DOFs is used, the expression of Eq. (26) is related to

$$\langle P_n(0)P_m(t)\rangle_{CMM}$$
$$= \int_{\sum_{n=1}^F P_n(0)=1} d\mathbf{x}(0)d\mathbf{p_x}(0)d\mathbf{y}(0)d\mathbf{p_y}(0)\mathrm{Tr}_{nuc}$$
$$\times \Big[\hat{\rho}_{nuc}P_n(0)\exp\Big(\frac{it}{\hbar}\hat{H}_{LM}\Big)P_m(0)\exp\Big(-\frac{it}{\hbar}\hat{H}_{LM}\Big)\Big]. \quad (27)$$

Here, the trace over the electronic DOFs is replaced by an integral over the mapping phase space $(\mathbf{x},\mathbf{p_x},\mathbf{y},\mathbf{p_y})$ with the constraint that the total population is 1. That is,

$$\sum_{n=1}^F P_n(0) = 1 \text{ and } 0 \le P_n(0) \le 1 \quad (\forall n). \quad (28)$$

This physical constraint is consistent with the implicit employment of Eq. (16) (the conservation of the total population) in deriving the Hamiltonian Eq. (23) or (24) from Eq. (22). The trace over the nuclear DOFs in Eq. (27) can be approximated by the conventional linearized semiclassical initial value representation (LSC-IVR),[40,84,85] which leads to

$$\langle P_n(0)P_m(t)\rangle_{CMM} = \int_{\sum_{n=1}^F P_n(0)=1} d\mathbf{x}(0)d\mathbf{p_x}(0)d\mathbf{y}(0)d\mathbf{p_y}(0)$$
$$\times \int d\mathbf{R}_0 d\mathbf{P}_0 \rho_W^{nuc}(\mathbf{R}_0,\mathbf{P}_0)P_n(0)P_m(t). \quad (29)$$

Here, ρ_W^{nuc} is the Wigner function of the density operator $\hat{\rho}_{nuc}$, i.e.,

$$\rho_W^{nuc}(\mathbf{R},\mathbf{P}) = \frac{1}{(2\pi\hbar)^f}\int d\Delta\exp\Big(i\mathbf{p}^T\Delta/\hbar\Big)\Big\langle \mathbf{R}-\frac{\Delta}{2}\Big|\hat{\rho}_{nuc}\Big|\mathbf{R}+\frac{\Delta}{2}\Big\rangle, \quad (30)$$

with f being the total nuclear DOFs and $P_m(t)$ is evaluated along the trajectory $(\mathbf{R}(t),\mathbf{P}(t);\mathbf{x}(t),\mathbf{p_x}(t),\mathbf{y}(t),\mathbf{p_y}(t))$ governed by Hamilton's equations of motion defined by the Hamiltonian Eq. (24). In Eq. (29), any initial (physical) condition that satisfies Eq. (28) is equally weighted (for the classical mapping Hamiltonian)

throughout the present paper. For convenience, the classical Li-Miller mapping model [Eq. (24) as the Hamiltonian] with Eq. (29) is denoted CMM1 (classical mapping model 1) in the rest of this paper. In Eq. (29) for CMM1, one has

$$P_m(t) = x^{(m)}(t)p_y^{(m)}(t) - y^{(m)}(t)p_x^{(m)}(t). \quad (31)$$

With the correlation function $\langle P_n(0)P_m(t)\rangle_{CMM}$ defined in classical mapping models (CMMs), the expression of the time-dependent transition probability Eq. (25) from state $|n\rangle$ to state $|m\rangle$ is obtained by the normalization procedure,

$$P_{m\leftarrow n}(t) = F(F+1)\langle P_n(0)P_m(t)\rangle_{CMM} - 1 \quad (\forall m). \quad (32)$$

Equation (32) is the counterpart of CMMs for Eq. (25) or (26) in quantum mechanics. (See Appendix A for more discussion.) When the initial electronic state is $|n\rangle$, the population of state $|m\rangle$ as a function of time is expressed as Eq. (32), while the population difference between state $|n\rangle$ and state $|m\rangle$ is obtained by $P_{n\leftarrow n}(t) - P_{m\leftarrow n}(t)$.

Similarly, the classical Meyer-Miller mapping model Eq. (8) leads to

$$\hat{H}_{MM} = \sum_{m,n=1}^F \frac{1}{2}\Big(x^{(n)}x^{(m)} + p^{(n)}p^{(m)}\Big)H_{nm}(\hat{\mathbf{R}},\hat{\mathbf{P}}). \quad (33)$$

The classical mapping Hamiltonian for both nuclear and electronic DOFs for Eq. (20) or (21) is then

$$H_{MM}(\mathbf{R},\mathbf{P};\mathbf{x},\mathbf{p}) = \sum_{m,n=1}^F \frac{1}{2}\Big(x^{(n)}x^{(m)} + p^{(n)}p^{(m)}\Big)H_{nm}(\mathbf{R},\mathbf{P}), \quad (34)$$

where $\mathbf{x}$ and $\mathbf{p}$ are the vectors for $\{x^{(n)}\}$ and $\{p^{(n)}\}$, respectively. The classical mapping Hamiltonian for both nuclear and electronic DOFs in the diabatic representation is

$$H_{MM}(\mathbf{R},\mathbf{P};\mathbf{x},\mathbf{p})$$
$$= \frac{1}{2}\mathbf{P}^T\mathbf{M}^{-1}\mathbf{P} + \sum_{n,m=1}^F \frac{1}{2}\Big(x^{(n)}x^{(m)} + p^{(n)}p^{(m)}\Big)V_{nm}(\mathbf{R}). \quad (35)$$

Note that the conservation of the total population Eq. (15) is implicitly used for the kinetic energy term in Eq. (35) when we derive Eq. (35) from Eq. (33) or (34). Similar to Eq. (29), replacing the trace over the electronic DOFs by an integral over the mapping phase space $(\mathbf{x},\mathbf{p})$ with the constraint that the total population is 1 [i.e., Eq. (28)], one obtains the expression of $\langle P_n(0)P_m(t)\rangle_{CMM}$ of CMM2,

$$\langle P_n(0)P_m(t)\rangle_{CMM} = \int_{\sum_{n=1}^F P_n(0)=1} d\mathbf{x}_0 d\mathbf{p}_0$$
$$\times \int d\mathbf{R}_0 d\mathbf{P}_0 \rho_W^{nuc}(\mathbf{R}_0,\mathbf{P}_0)P_n(0)P_m(t), \quad (36)$$

in Eq. (32) for evaluating Eq. (25) or (26) in quantum mechanics. Here, $P_m(t)$ is estimated along the trajectory $(\mathbf{R}(t),\mathbf{P}(t);\mathbf{x}(t),\mathbf{p}(t))$, the equations of motion of which are governed by the Hamiltonian Eq. (35). In the present paper, any initial condition subject to the physical population constraint [i.e., Eq. (28)] is equally treated. For convenience, the classical Meyer-Miller model [Eq. (35) as the Hamiltonian] with Eq. (36) is denoted as CMM2 (classical mapping model 2) in the rest of this paper. In CMM2, Eq. (32) is also the expression of the time-dependent transition probability Eq. (25)

from state $|n\rangle$ to state $|m\rangle$). By following Eqs. (27)–(30) and (32), it is trivial to extend the formulation to other phase space mapping models in the unified framework.

Below we investigate the performance of CMMs with various numerical example tests in the condensed phase. For fair comparison, we also use the MFT (mean field trajectory) method, where the initial condition for the nuclear DOFs is sampled from the normalized Wigner distribution for the initial density operator for the bath modes (as done in the LSC-IVR) and then each trajectory is propagated by the conventional Ehrenfest dynamics.

III. RESULTS AND DISCUSSIONS

A. Spin-boson model

The spin-boson model describes a two-state system coupled to an environmental harmonic bath, serving as a simple yet[86] challenging model that includes most key aspects of dissipative quantum systems.[87] Benchmark dynamics or thermodynamics results of the spin-boson model have been achieved by several exact quantum approaches, including the numerically exact quasiadiabatic propagator path integral (QuAPI) of Makri and co-workers,[88–92] multi-configuration time-dependent Hartree (MCTDH),[93–98] hierarchical equations of motion (HEOM),[99–105] and multi-electronic-state path integral molecular dynamics (MES-PIMD)[106,107].

The Hamiltonian operator of the spin-boson model is often described by

$$\hat{H} = \sum_j \frac{1}{2}\left(\hat{P}_j^2 + \omega_j^2 \hat{R}_j^2\right) + \left(\sum_j c_j \hat{R}_j\right)\hat{\sigma}_z + \varepsilon\hat{\sigma}_z + \Delta\hat{\sigma}_x, \quad (37)$$

where R_j and P_j are the mass-weighted position and momentum of the jth mode of the harmonic bath, ε is the energy bias of the two states, Δ is the tunneling matrix element of the two states, and $\hat{\sigma}_x$ and $\hat{\sigma}_z$ are the x-component and z-component of the Pauli operators, respectively. In Eq. (37), frequencies and coupling coefficients $\{\omega_j, c_j\}$ are sampled from a specific spectral density function for the bath.

A typical kind of bath is the Ohmic bath,[87] of which the spectral density is

$$J(\omega) = \frac{\pi}{2}\alpha\omega f\left(\frac{\omega}{\omega_c}\right)\Theta(\omega), \quad (38)$$

where $\Theta(\omega)$ is a Heaviside function, α is the dimensionless Kondo parameter, and $f(\omega/\omega_c)$ stands for a cutoff function for the linear spectrum density, which usually employs an exponential form $f(\omega/\omega_c) = e^{-\omega/\omega_c}$. That is, for $\omega \geq 0$, the spectral density function Eq. (38) of the Ohmic bath takes the form

$$J(\omega) = \frac{\pi}{2}\alpha\omega e^{-\omega/\omega_c}. \quad (39)$$

Another typical kind is the Debye bath[93,108,109] [which can be viewed as Eq. (38) with a Lorentzian cutoff], of which the spectral density reads

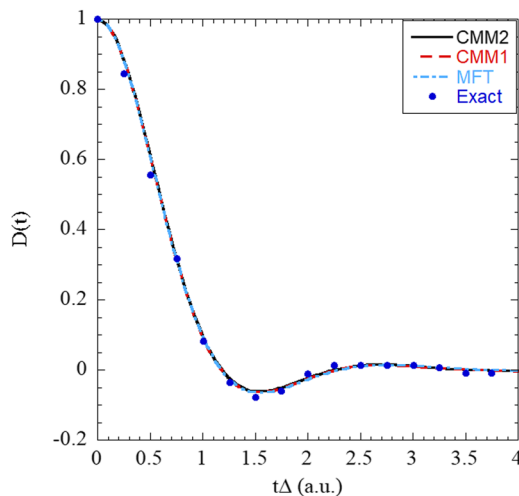$$J(\omega) = 2\lambda\frac{\omega_c\omega}{\omega_c^2 + \omega^2}. \quad (40)$$

FIG. 1. Population difference [defined as $D(t) = P_{1\leftarrow1}(t) - P_{2\leftarrow1}(t)$] of the spin-boson Hamiltonian with the Ohmic bath as a function of time. The initial state is set to $|1\rangle$. Model 1 is a symmetric spin-boson model with the parameters $\varepsilon = 0$, $\Delta = 0.1$, $\beta = 1$, $\omega_c = 0.25$, $\alpha = 0.09$, $dt = 0.01$, and $N_b = 50$. The model leads to typical incoherent relaxation dynamics. Black solid line shows results produced by the classical Meyer-Miller mapping model (CMM2, classical mapping model 2), red dashed line illustrates results yielded by the classical Li-Miller mapping model (CMM1, classical mapping model 1), and light blue dotted-dashed line depicts results given by the mean-field trajectory (MFT) method. Exact results (produced by QuAPI in Ref. 88) are shown in dark blue solid circles.

Here, ω_c is the characteristic frequency of the bath and λ denotes the reorganization energy.[49,110]

In numerical simulations for the spin-boson Hamiltonian Eq. (37), we discretize the continuous bath into the conventional
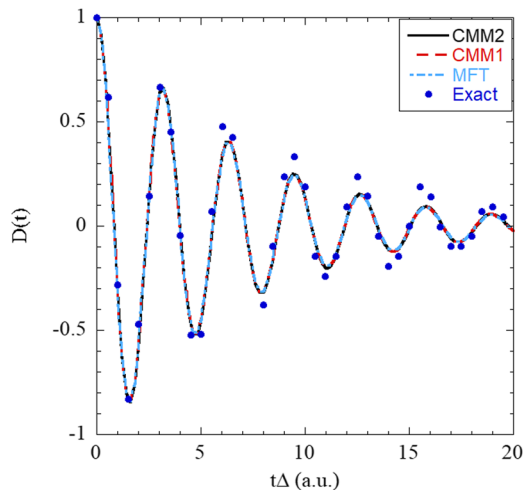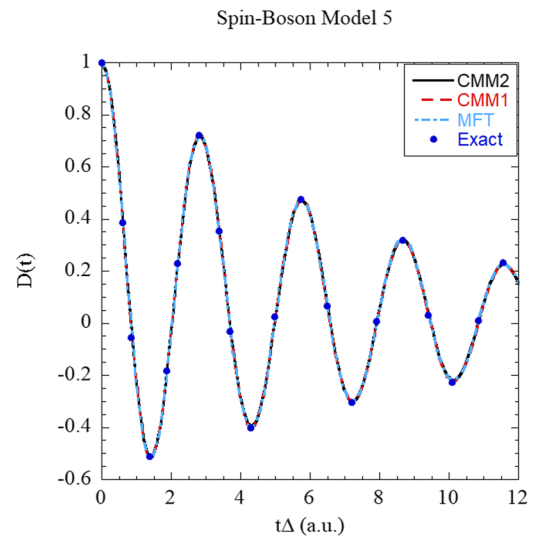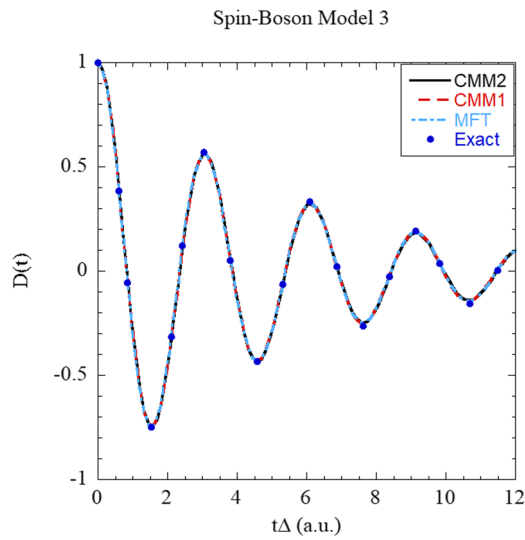

FIG. 2. Same as in Fig. 1, but for model 2, of which all parameters are the same as those of model 1, except a relative low temperature $\beta = 50$. The exact data (produced by QuAPI) are taken from Ref. 88.

FIG. 3. Same as in Fig. 1, but for model 3, of which the parameters are $\varepsilon = 0$, $\Delta = 1$, $\beta = 0.25$, $\omega_c = 5$, $\alpha = 0.02$, $dt = 0.01$, and $N_b = 50$. Exact data (produced by MCTDH) are taken from Ref. 94.

FIG. 5. Same as in Fig. 3, but for $\omega_c = 0.25$, $\alpha = 0.4$, and $N_b = 100$. (Model 5) Exact data (produced by MCTDH) are taken from Ref. 94.

form[40,62,87,109]

$$J(\omega) = \frac{\pi}{2} \sum_{j=1}^{N_b} \frac{c_j^2}{\omega_j} \delta(\omega - \omega_j). \tag{41}$$

In this paper, we adopt the discretization scheme in Refs. 56 and 111–115, i.e.,

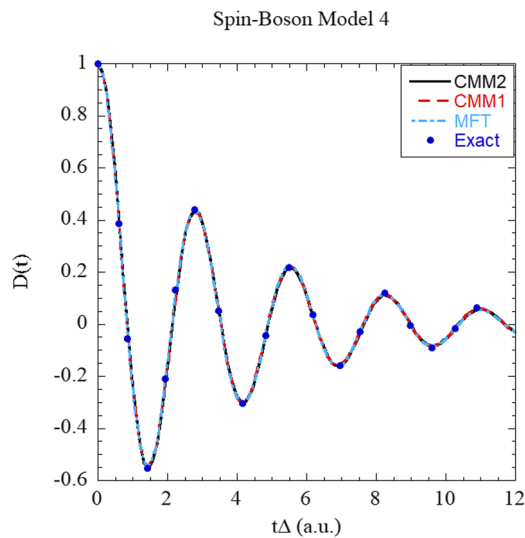$$c_j^2 = \frac{2}{\pi} \omega_j \frac{J(\omega_j)}{\rho(\omega_j)}, \tag{42}$$

with $\rho(\omega)$ satisfying

$$\int_0^{\omega_j} d\omega \rho(\omega) = j. \tag{43}$$

Choosing $\rho(\omega) \propto (N_b + 1) e^{-\omega/\omega_c}/\omega_c$ for the Ohmic bath leads to[114,115]

$$\omega_j = -\omega_c \ln[1 - j/(1 + N_b)], \quad j = 1, \ldots, N_b, \tag{44}$$

$$c_j = \sqrt{\frac{\alpha \omega_c}{N_b + 1}} \omega_j, \quad j = 1, \ldots, N_b, \tag{45}$$

FIG. 4. Same as in Fig. 3, but for $\omega_c = 1$ and $\alpha = 0.1$. (Model 4) Exact data (produced by MCTDH) are taken from Ref. 94.

FIG. 6. Same as in Fig. 1, but for an asymmetric case (model 6), of which the parameters are $\varepsilon = 1$, $\Delta = 1$, $\beta = 0.25$, $\omega_c = 1$, $\alpha = 0.4$, $dt = 0.01$, and $N_b = 100$. Exact data (produced by MCTDH) are taken from Ref. 94.
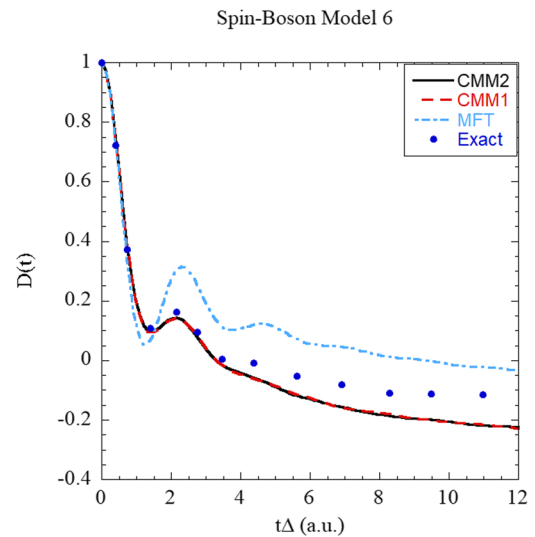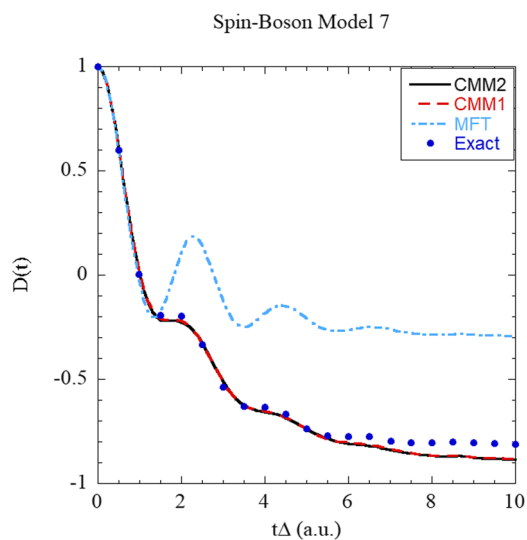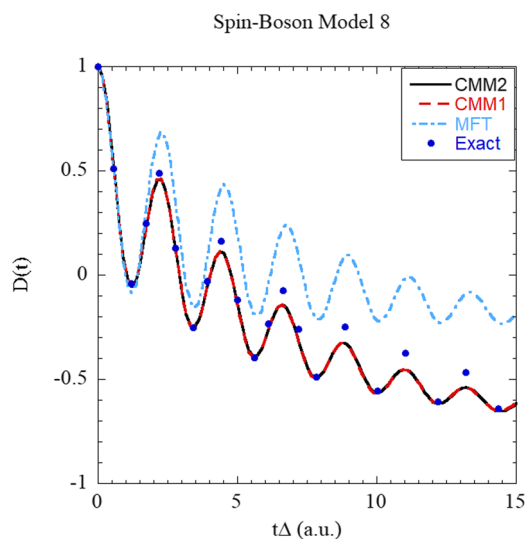
FIG. 7. Same as in Fig. 6, but for $\beta = 5$, $\omega_c = 2$, and $N_b = 50$. (Model 7) Exact data (produced by QuAPI) are taken from Ref. 116.

FIG. 9. Same as in Fig. 8, but for $\alpha = 0.2$. (Model 9) Exact data (produced by MCTDH) are taken from Ref. 94.

where N_b is the number of discretized bath modes. In this paper, we take $\rho(\omega) \propto (N_b + 1)/(\omega^2 + \omega_c^2)$ for the Debye bath, which yields[114]

$$\omega_j = \omega_c \tan\left(\frac{\pi}{2}\left(1 - \frac{j}{N_b + 1}\right)\right), \quad j = 1, \ldots, N_b, \qquad (46)$$

$$c_j = \sqrt{\frac{2\lambda}{N_b + 1}}\,\omega_j, \quad j = 1, \ldots, N_b. \qquad (47)$$

The spin-boson model is symmetric when $\varepsilon = 0$ and asymmetric when $\varepsilon \neq 0$. Different dynamics regimes can be accessed by choosing a variety of parameters: $\beta\Delta \leq 1$ often describes the relatively high

temperature region, while $\beta\Delta > 1$ indicates relatively low temperature cases; $\omega_c \leq \Delta$ usually corresponds to the adiabatic regime, while $\omega_c > \Delta$ implies the nonadiabatic domain. The Kondo parameter α or reorganization energy λ depicts the system-bath coupling strength. The larger α or λ is, the stronger coupling between the system and bath is.

In all numerical simulations for the spin-boson model throughout this paper, the initial density is a product of the density of the system (i.e., the electronic DOFs) and that of the bath modes (i.e., the nuclear DOFs). The initial condition for the electronic DOFs is the excited state of the system (i.e., $|1\rangle$, a pure state). The initial density

FIG. 8. Same as in Fig. 1, but for model 8, of which the parameters are $\varepsilon = 1$, $\Delta = 1$, $\beta = 5$, $\omega_c = 2.5$, $\alpha = 0.1$, $dt = 0.01$, and $N_b = 50$. Exact data (produced by MCTDH) are taken from Ref. 94.
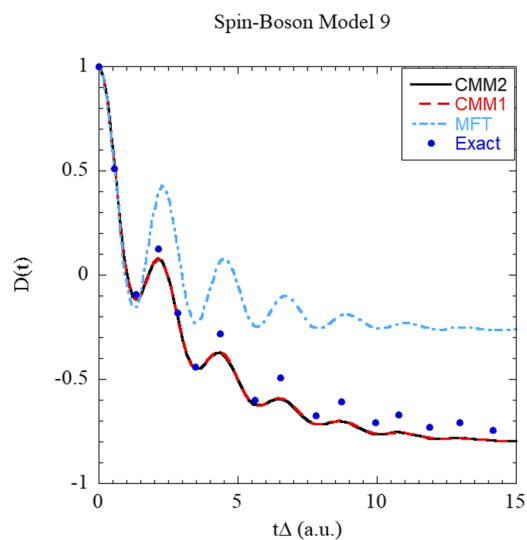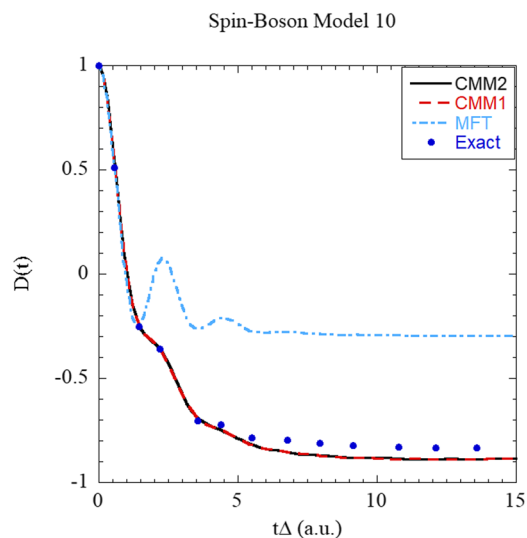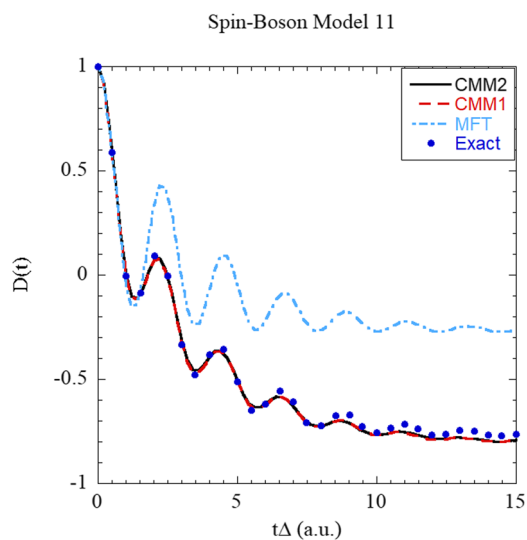

FIG. 10. Same as in Fig. 8, but for $\alpha = 0.4$, $N_b = 100$. (Model 10) Exact data (produced by MCTDH) are taken from Ref. 94.

FIG. 11. Same as in Fig. 1, but for model 11, of which the parameters are $\varepsilon = 1$, $\Delta = 1$, $\beta = 10$, $\omega_c = 2.5$, $\alpha = 0.2$, $dt = 0.01$, and $N_b = 50$. Exact data (produced by QuAPI) are taken from Ref. 86.
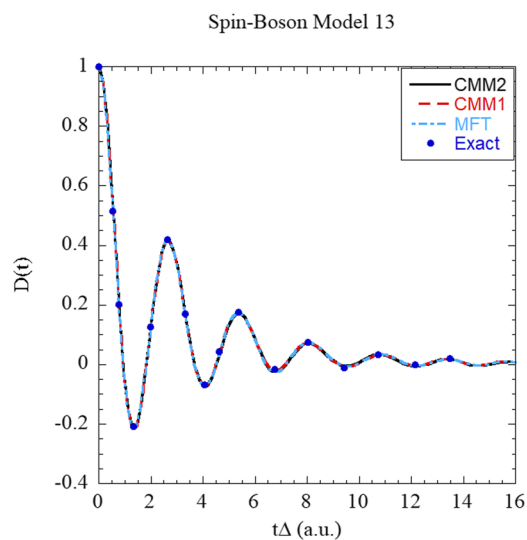

FIG. 13. Same as in Fig. 12, but for $\lambda = 0.25$ (model 13). Exact data (produced by MCTDH) are taken from Ref. 93.

of the nuclear DOFs is

$$\hat{\rho}_{nuc} = e^{-\beta \hat{H}_b} / Z_b, \tag{48}$$

where the bare bath Hamiltonian is

$$\hat{H}_b = \sum_{j=1}^{N_b} \frac{1}{2} \left(\hat{P}_j^2 + \omega_j^2 \hat{R}_j^2 \right) \tag{49}$$

and $Z_b = \text{Tr}_{nuc}\left[e^{-\beta \hat{H}_b} \right]$ is the partition function for the harmonic bath. The normalized Wigner distribution for the initial density Eq. (48) is

$$\rho_W^{nuc}(\mathbf{R}, \mathbf{P}) = \prod_{j=1}^{N_b} \frac{\tanh\left(\frac{1}{2} \beta \hbar \omega_j \right)}{\pi \hbar} \exp\left[-\frac{\beta}{2Q(\omega_j)} \left(P_j^2 + \omega_j^2 R_j^2 \right) \right], \tag{50}$$
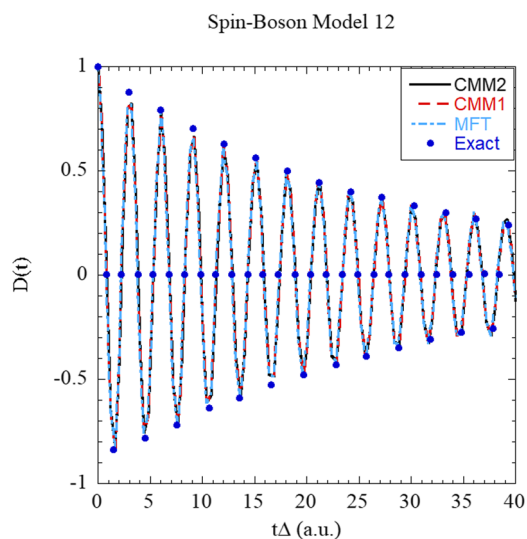

FIG. 12. Same as in Fig. 1, but for a symmetric spin-boson model with the Debye bath (model 12), of which the parameters are $\varepsilon = 0$, $\Delta = 1$, $\beta = 0.5$, $\omega_c = 0.25$, $\lambda = 0.025$, $dt = 0.002$, and $N_b = 100$. Exact data (produced by MCTDH) are taken from Ref. 93.
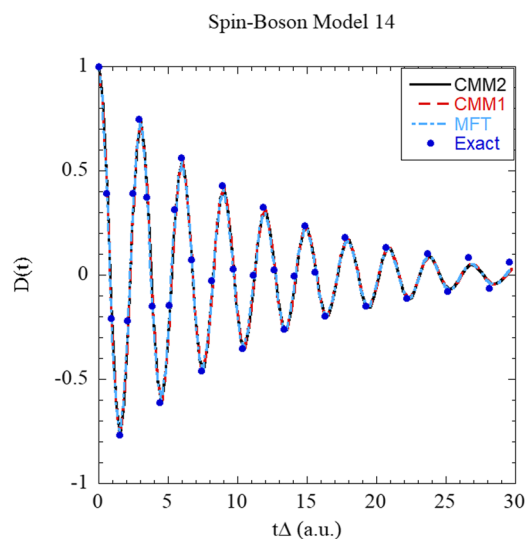

FIG. 14. Same as in Fig. 12, but for model 14 that uses a set of parameters $\varepsilon = 0$, $\Delta = 1$, $\beta = 5$, $\omega_c = 0.25$, $\lambda = 0.25$, and $dt = 0.002$. Exact data (produced by MCTDH) are taken from Ref. 93.
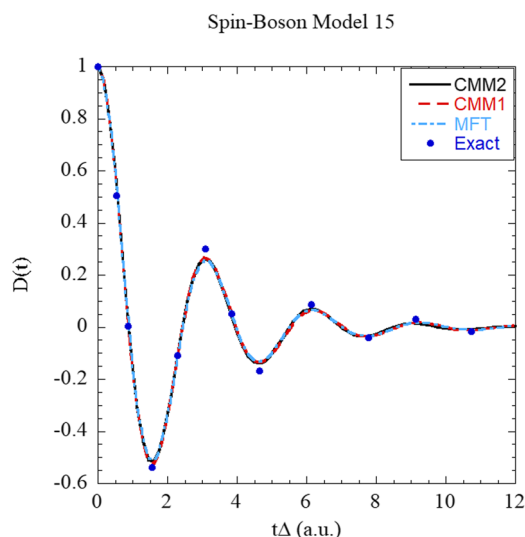
FIG. 15. Same as in Fig. 12, but for model 15, of which the parameters are $\varepsilon = 0$, $\Delta = 1$, $\beta = 0.5$, $\omega_c = 5$, $\lambda = 0.25$, $dt = 0.002$, and $N_b = 100$. Exact data (produced by MCTDH) are taken from Ref. 93.

where the quantum corrector[85] $Q(\omega_j)$ is defined as

$$Q(\omega_j) = \frac{\frac{1}{2}\beta\hbar\omega_j}{\tanh\left(\frac{1}{2}\beta\hbar\omega_j\right)}. \tag{51}$$

1. Spin-boson model with the Ohmic bath

We test 11 spin-boson models where the Ohmic bath is used. The available benchmark exact results are obtained from QuAPI[88] or MCTDH.[94] All simulations employ an ensemble of 10^6 trajectories
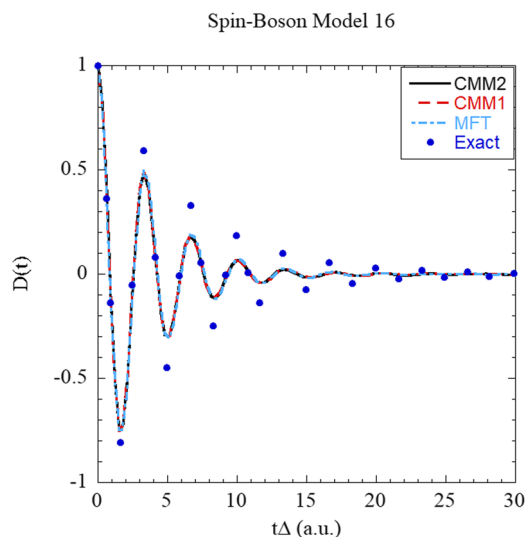

FIG. 16. Same as in Fig. 15, but for $\beta = 50$. Exact data (produced by MCTDH) are taken from Ref. 93.
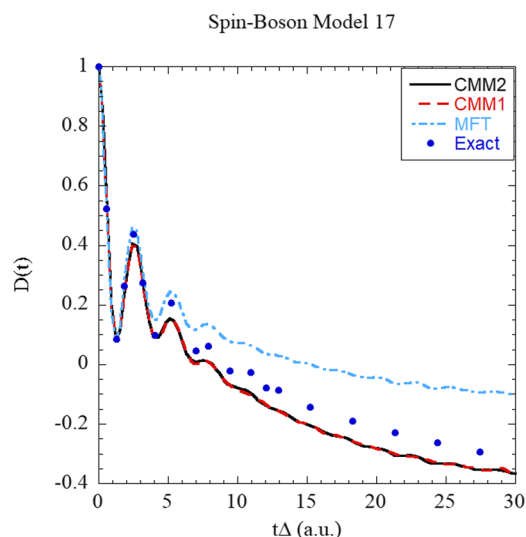

FIG. 17. Same as in Fig. 12, but for an asymmetric spin-boson model with the Debye bath (model 17), whose parameters are $\varepsilon = 1$, $\Delta = 1$, $\beta = 0.5$, $\omega_c = 0.25$, $\lambda = 0.25$, $dt = 0.002$, and $N_b = 100$. Exact data (produced by MCTDH) are taken from Ref. 93.

and adapt a time step of $dt = 0.01$. Here, all parameters are in atomic units (a.u.).

a. Symmetric cases. The first five models (models 1–5) are symmetric spin-boson models in the literature. In models 1–2 (from Ref. 88), the characteristic frequency $\omega_c = 2.5\Delta$ (in the nonadiabatic regime with a fast bath) and the Kondo parameter $\alpha = 0.09$ are used. Model 1 lies in a relatively high temperature regime ($\beta\Delta = 0.1$), demonstrating relaxation dynamics with incoherent decay. Model
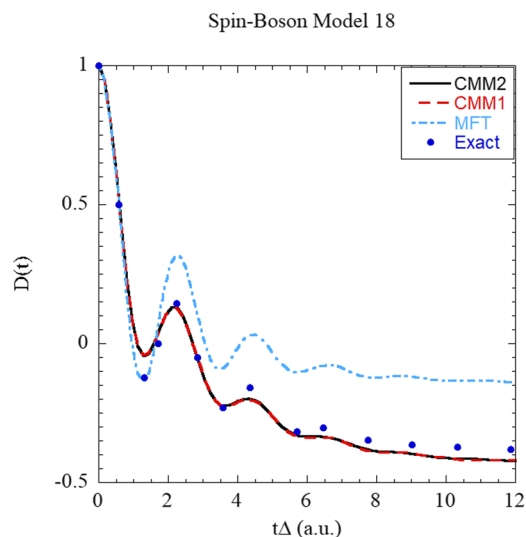

FIG. 18. Same as in Fig. 17, but for $\omega_c = 5$. Exact data (produced by MCTDH) are taken from Ref. 93.
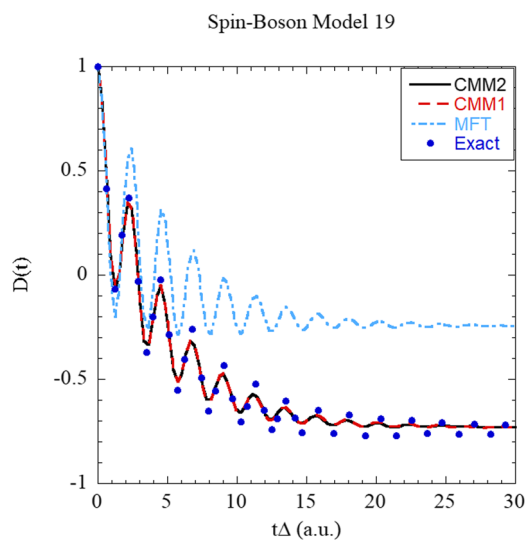
Spin-Boson Model 19

FIG. 19. Same as in Fig. 17, but for β = 50 and ω_c = 5. Exact data (produced by MCTDH) are taken from Ref. 93.

2 employs a relatively low temperature ($\beta\Delta$ = 5), exhibiting coherent dynamics with more oscillatory behaviors. Models 3–5 show a high temperature case $\beta\Delta$ = 0.25 with a series of Kondo parameters α = 0.02, 0.1, 0.4 (with $\alpha\omega_c$ = 0.1 fixed).[94] Figures 1–5 suggest that CMMs lead to nearly the same results as MFT produces for symmetric spin-boson models. The results are in excellent agreement with the exact data in the high temperature regime as shown in Figs. 1 and 3–5. In the low temperature regime in Fig. 2, CMMs as well as MFT also demonstrate overall good performance. The results can produce accurate oscillation frequencies, although their amplitudes are slightly less accurate in the long time limit.

In all symmetric cases, CMMs and MFT share similar numerical behaviors and provide a good description on real time dynamics.

b. Asymmetric cases. Models 6–11 are more challenging asymmetric spin-boson models with the Ohmic bath studied in the literature. Model 6 shows a case on the boundary of the adiabatic and nonadiabatic regions (ω_c = Δ), which involves a relatively high temperature ($\beta\Delta$ = 0.25) and a relatively strong system-bath coupling (α = 0.4). Figure 6 shows that CMMs yield reasonably accurate results in the high temperature region, while the performance of MFT is slightly worse. Model 7 (from Ref. 116) is a case with the same strong system-bath coupling strength (α = 0.4) but in the nonadiabatic region (ω_c = 2Δ) with a lower temperature ($\beta\Delta$ = 5). Figure 7 demonstrates that CMMs are capable of reproducing the
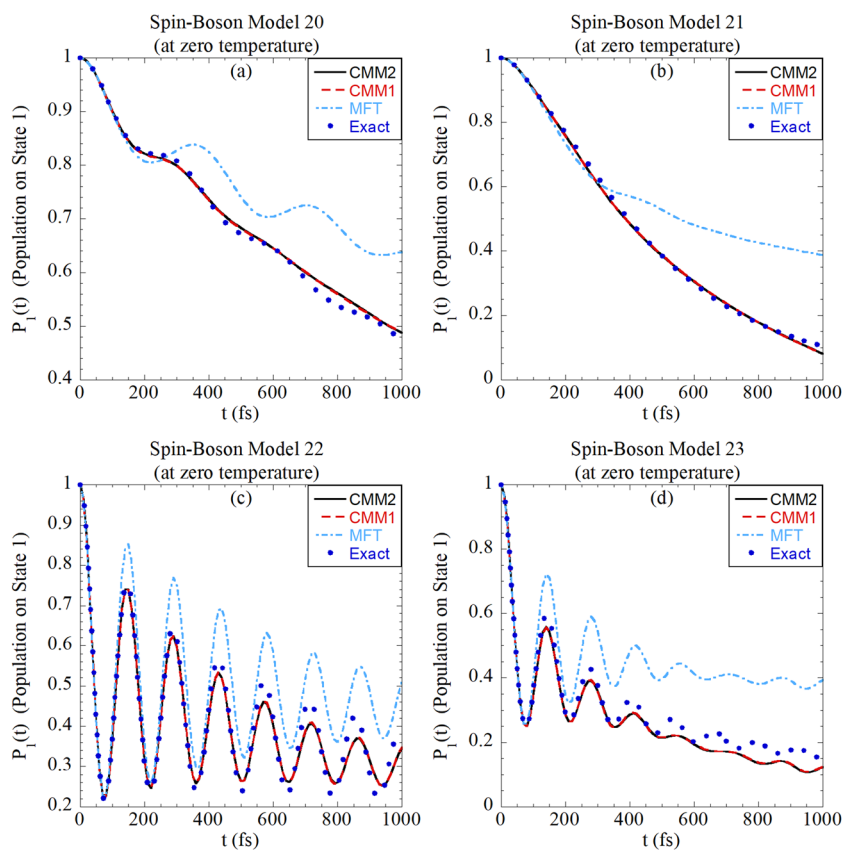

FIG. 20. Population of State 1 as a function of time, which is expressed by Eq. (32) in CMMs for four spin-boson models at zero temperature (from Ref. 104), with a biased spin system (ε = 50 cm^{-1}) coupled with a quantum Ohmic bath, whose parameters are the characteristic frequency ω_c = 10 ps^{-1} = 53.09 cm^{-1}, (a) α = 0.3767, Δ = 20 cm^{-1}; (b) α = 1.130, Δ = 20 cm^{-1}; (c) α = 0.7535, Δ = 100 cm^{-1}; and (d) α = 1.884, Δ = 100 cm^{-1}. Black solid line shows results produced by the classical Meyer-Miller mapping model (CMM2, classical mapping model 2), red dashed line illustrates results yielded by the classical Li-Miller mapping model (CMM1, classical mapping model 1), and light blue dotted-dashed line depicts results given by the mean-field trajectory (MFT) method. Exact results (produced by ML-MCTDH in Ref. 104) are showed in dark blue solid circles.

critical damping behavior as well as the asymptote in the long time limit of the exact results (by QuAPI in Ref. 116) in this spin-boson model. MFT begins to notably deviate from the exact data since fairly short time $t\Delta = 1$ a.u. and leads to more significant failure for achieving the correct asymptotic behavior as time increases. More serious tests are made in Figs. 8–10 for models 8–10 in the low temperature domain ($\beta\Delta = 5$) and in the deeper nonadiabatic region $\omega_c = 2.5\Delta$), in which the Kondo parameters $\alpha = 0.1, 0.2, 0.4$ range from the weak to strong system-bath coupling domains (from Ref. 94). Figures 8–10 demonstrate that the discrepancy between the performance of CMMs and that of MFT is much more distinct. It is encouraging that CMMs are able to capture the asymptotic behaviors in the long limit, showing an overall reasonably good agreement with exact results. For comparison, MFT fails to reach the correct long-time asymptote of the population difference in all three cases—the stronger the system-bath coupling strength is, the worse the numerical performance of MFT is. Figure 11 shows numerical results for model 11, which lies in the nonadiabatic region ($\omega_c = 2.5\Delta$) with an even lower temperature ($\beta\Delta = 10$) and with the Kondo parameter $\alpha = 0.2$ (from Ref. 86). The accuracy of CMMs with respect to the exact results is practically satisfying. They are able to offer a much better illustration of the behaviors in the asymptotic limit than MFT does.

In all asymmetric cases, CMMs produce reasonably accurate results in the short limit as well as in the long-time asymptotic limit, while MFT fails to capture the correct asymptotic behaviors—it becomes progressively worse as the temperature is lower, the system-bath coupling is stronger, and/or the deeper the nonadiabatic region is.

2. Spin-boson model with the Debye bath

Comparing Eq. (40) to Eq. (39), it is straightforward to see that the Debye bath spans a much broader frequency range than the conventional Ohmic bath, which presents more challenging tests for nonadiabatic dynamics methods. Eight spin-boson models with the Debye bath (models 12–19) reported in the literature[93] are used for demonstration. [Comparison between Eq. (40) of this paper and Eq. (2.24) of Ref. 93 defines the value of λ for these models.] All simulations employ an ensemble of 10^6 trajectories and adapt a time step of $dt = 0.002$. (Parameters are in atomic units.)

a. Symmetric cases. Models 12–14 are all symmetric cases in the adiabatic regime ($\omega_c = 0.25\Delta$). Model 12 is at a relatively high temperature $\beta\Delta = 0.5$ with the reorganization energy $\lambda = 0.025$ (i.e., relatively weak system-bath coupling), model 13 represents a case with a larger reorganization energy $\lambda = 0.25$ (i.e., relatively strong

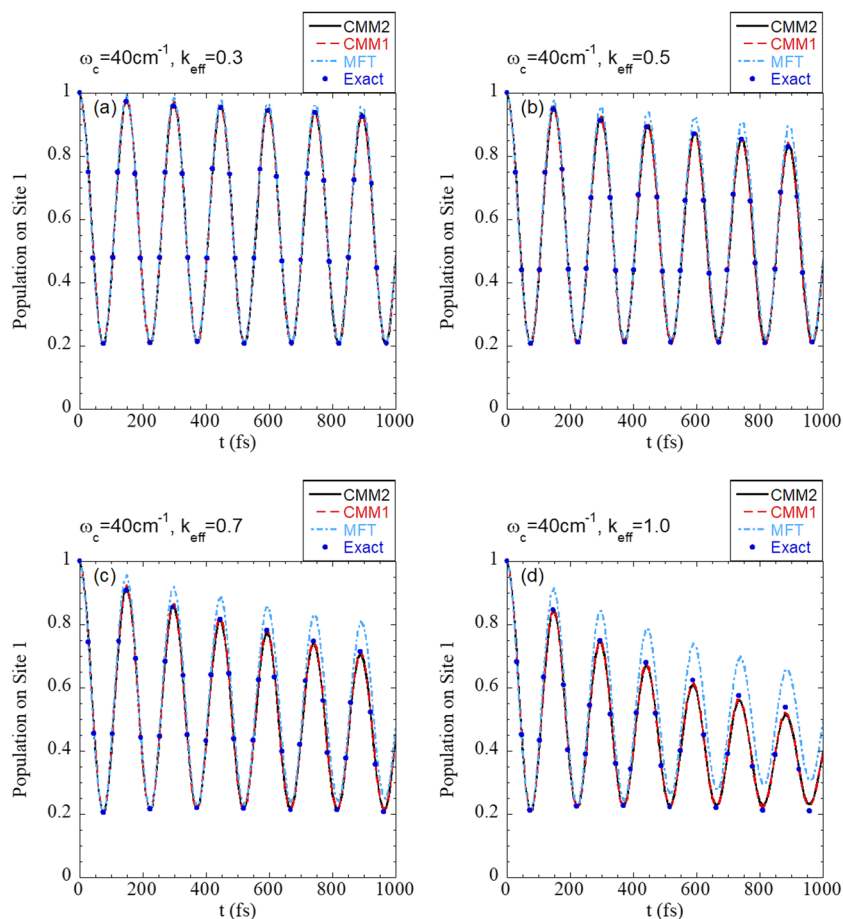**FIG. 21.** Population of site 1 as a function of time, which is expressed by Eq. (32) in CMMs for an asymmetric site-exciton model, where $\Delta E = V_{12} = 0.0124$ eV, $\omega_c = 40$ cm^{-1}, and $N_b = 100$, with different couplings (a) $k_{eff} = 0.3$, (b) $k_{eff} = 0.5$, (c) $k_{eff} = 0.7$, or (d) $k_{eff} = 1.0$. Markers are used in the same way as in Fig. 1. Exact data (produced by MCTDH) are provided by Ref. 83.

system-bath coupling) in the high temperature region ($\beta\Delta = 0.5$), and model 14 is in the low temperature ($\beta\Delta = 5$) region with $\lambda = 0.25$. All simulation results in comparison to exact data are demonstrated in Figs. 12–14. Both CMMs and MFT lead to similar results that are in overall good agreement with the counterpart exact data. As shown in the comparison between Figs. 13 and 14, numerical results of CMMs become less accurate in the long time limit when the temperature decreases.

Models 15–16 are two symmetric examples in the nonadiabatic regime ($\omega_c = 5\Delta$) with the reorganization energy $\lambda = 0.25$, one in the high-temperature regime ($\beta\Delta = 0.5$), the other in the low-temperature domain ($\beta\Delta = 50$). Figure 15 shows that CMMs and MTF exhibit excellent numerical performance in the high-temperature regime for symmetric cases in the nonadiabatic domain. In contrast, Fig. 16 suggests that CMMs and MTF lead to less accurate results in the low-temperature regime—they produce practically accurate oscillation frequencies but their amplitudes are notably smaller than the exact data.

In all symmetric cases, CMMs and MFT demonstrate very similar numerical performance and provide reasonably good approximations to exact quantum dynamics in the adiabatic and nonadiabatic regions.

b. Asymmetric cases. Asymmetric spin-boson models with the Debye bath are often more challenging benchmark tests than symmetric ones. We focus on three asymmetric cases (in Ref. 93) with the bias $\varepsilon = 1$ and the reorganization energy $\lambda = 0.25$, in which model 17 is in the adiabatic region ($\omega_c = 0.25\Delta$) and in the high-temperature region ($\beta\Delta = 0.5$), model 18 is in the nonadiabatic region ($\omega_c = 5\Delta$) and in the high-temperature region ($\beta\Delta = 0.5$), and model 19 represents another case in the nonadiabatic region ($\omega_c = 5\Delta$) but in the low-temperature region ($\beta\Delta = 50$).

Figures 17–19 reveal that CMMs demonstrate significantly different numerical performance from MFT for all three asymmetric cases, irrespective of whether the spin-boson model is in the adiabatic or nonadiabatic region. MFT shows poor performance for long time dynamics in the three cases demonstrated in Figs. 17–19. In contrast, CMMs are competent approaches to recover most behaviors in the asymptotic limit of long time quantum dynamics for all three asymmetric spin-boson models with the Debye bath.

3. Spin-boson model at zero temperature

Dynamics of the spin-boson model at zero temperature is much more challenging.[87] Numerical simulations usually confront
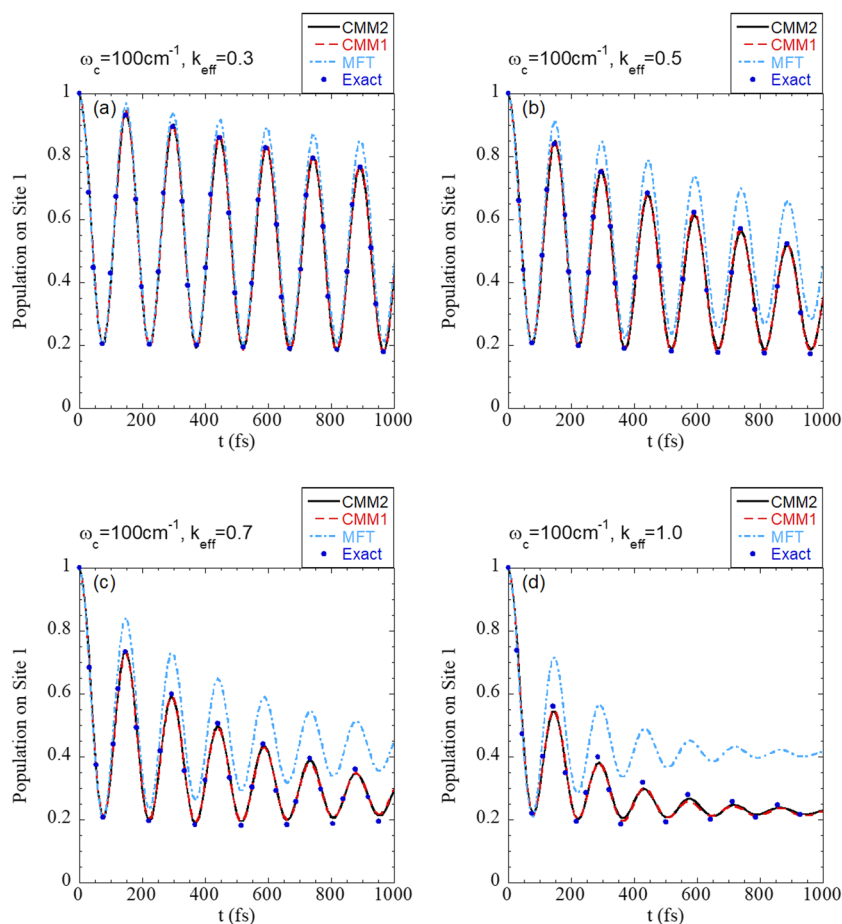

FIG. 22. Same as in Fig. 21, but for ω_c = 100 cm^{-1}. Exact data (produced by MCTDH) are taken from Ref. 83.

slow convergence problems.[97,98,104,117] Multilayer MCTDH (ML-MCTDH)[96] and numerical renormalization group[118] have provided benchmark results for some spin-boson models. Four asymmetric spin-boson models with the Ohmic bath (models 20–23) at zero temperature from Ref. 104 are tested for CMMs and MTF. All simulations employ an ensemble of 10^6 trajectories and adapt a time step of 0.1 fs, with the number of discretized bath modes $N_b = 100$. The benchmark exact results (for the population of state 1) are produced by ML-MCTDH in Ref. 104.

Comparison of Eq. (39) of this paper to Eq. (13) of Ref. 104 produces the value of the Kondo parameter α of the Ohmic bath used in this paper. Models 20–21 are in the nonadiabatic region ($\omega_c \approx 2.65\ \Delta$). The system-bath coupling of model 20 is $\alpha = 0.3767$, and that of model 21 is much stronger ($\alpha = 1.130$). As shown in Fig. 20(a) (for model 20) in comparison to ML-MCTDH, both CMMs and MFT work well until 100 fs, but MFT demonstrates poor performance after 150 fs while CMMs almost faithfully reproduce the exact results up to 1000 fs. In Fig. 20(b) (for model 21), the discrepancy between the MFT results and the exact ones becomes severe after 300 fs. In contrast, CMMs show overall good agreement with the exact results even in the long-time region.

Models 22–23 are in the adiabatic region ($\omega_c = 0.53\ \Delta$). The amplitude of the oscillation of the population dynamics decays faster as the system-bath coupling increases, as shown in the comparison between Fig. 20(c) (for model 22 with $\alpha = 0.7535$) and Fig. 20(d) (for model 23 with $\alpha = 1.884$). MFT works reasonably well for only the first half of the first oscillation and fails to capture long time behaviors. For comparison, the accuracy of the results yielded by CMMs is significantly more satisfying even at zero temperature.

Regardless of whether the Ohmic or Debye bath is used for the spin-boson model, and irrespective of whether finite temperature or more challenging zero temperature is employed, CMMs offer reasonably accurate approaches to study real time dynamics in most regions as suggested in Figs. 1–20 (especially in asymmetric cases in Figs. 7–11 and 17–20).

B. Site-exciton model

The site-exciton model has been widely applied to study photoinduced electronic energy transfer processes.[44,83,110,119–123] The Hamiltonian operator of the site-exciton model consists of three terms,

$$\hat{H} = \hat{H}_s + \hat{H}_b + \hat{H}_{sb}. \qquad (52)$$

In this paper $\hat{H}_s$ of Eq. (52) describes a system of two localized (electronic) states, of which the diabatic representation reads
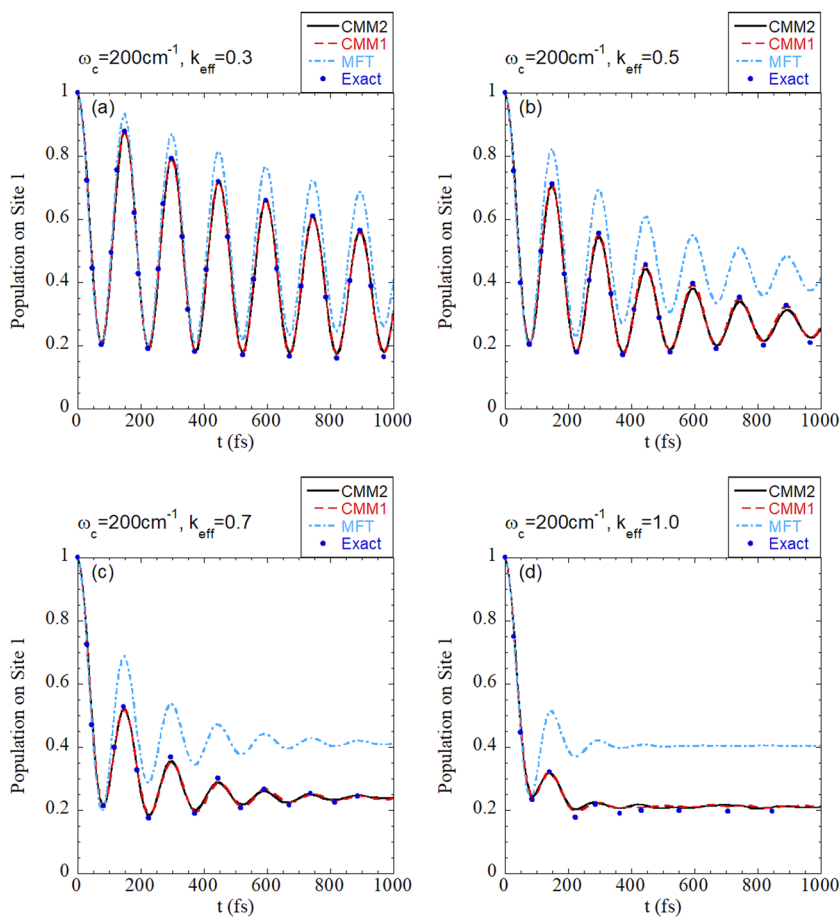

FIG. 23. Same as in Fig. 21, but for $\omega_c = 200\ \text{cm}^{-1}$. Exact data (produced by MCTDH) are taken from Ref. 83.

$$\hat{H}_s = \sum_{k=1}^{2} |\phi_k\rangle E_k \langle\phi_k| + \sum_{l\neq k}^{2} |\phi_k\rangle V_{kl} \langle\phi_l|. \qquad (53)$$

The bare bath Hamiltonian $\hat{H}_b$ of Eq. (52) is often depicted by the conventional harmonic bath (for the phonon modes) which takes the form

$$\hat{H}_b = \sum_{k=1}^{2} \sum_{j}^{N_b} \frac{1}{2} \left(\hat{P}_{kj}^2 + \omega_{kj}^2 \hat{R}_{kj}^2 \right). \qquad (54)$$

The Debye spectral density function is employed for Eq. (54) in this paper. (That is, Eq. (40) and the discretization algorithm (46)–(47) are used.) In Eq. (52), $\hat{H}_{sb}$ denotes the electron-phonon (system-bath) coupling that is represented by a bilinear function,

$$\hat{H}_{sb} = -\sum_{k=1}^{2} |\phi_k\rangle\langle\phi_k| \sum_{j}^{N_b} c_{kj} \hat{R}_{kj}. \qquad (55)$$

A dimensionless parameter k_{eff} defined in the literature,[83,123]

$$k_{eff} = \sqrt{2\lambda/\omega_c}, \qquad (56)$$

is employed to characterize the effective electron-phonon coupling. While the initial condition of the system is prepared on site 1

(i.e., $|\phi_1\rangle$), the initial density of the phonon DOFs (i.e., the bath modes) is given by the Boltzmann operator of the bare bath Hamiltonian at zero temperature. Its normalized Wigner distribution is

$$\rho_W^{nuc}(\mathbf{R}, \mathbf{P}) = \frac{1}{(\pi\hbar)^{N_b}} \prod_{j=1}^{N_b} \exp\left[-\frac{1}{\hbar\omega_j} \left(P_j^2 + \omega_j^2 R_j^2 \right) \right]. \qquad (57)$$

We consider asymmetric site-exciton models, in which the energy difference between the two sites is fixed at $\Delta E = E_1 - E_2 = 0.0124$ eV and the off-diagonal coupling between the two sites stays the same as $V_{12} = 0.0124$ eV. The dimensionless parameter k_{eff} (for the electron-phonon coupling) is 0.3, 0.5, 0.7, or 1.0. The characteristic frequency ω_c is 40 cm^{-1}, 100 cm^{-1}, 200 cm^{-1}, or 500 cm^{-1}, which ranges from the adiabatic region to the intermediate region, and then to the nonadiabatic region. In all site-exciton models, we employ $N_b = 100$ discretized bath modes.

Fully converged results (of CMMs) for the population of site 1 (i.e., $|\phi_1\rangle$) for all the site-exciton models in this paper are obtained with an ensemble of ~10^5 trajectories, each of which employs an integration time step $dt = 0.01$ fs for nuclear DOFs and $\delta t = 0.1 dt$ for underlying mapping electronic DOFs. Figures 21–24 demonstrate the comparison of the results produced by CMMs as well as by MTF to the corresponding exact data yielded by MCTDH.
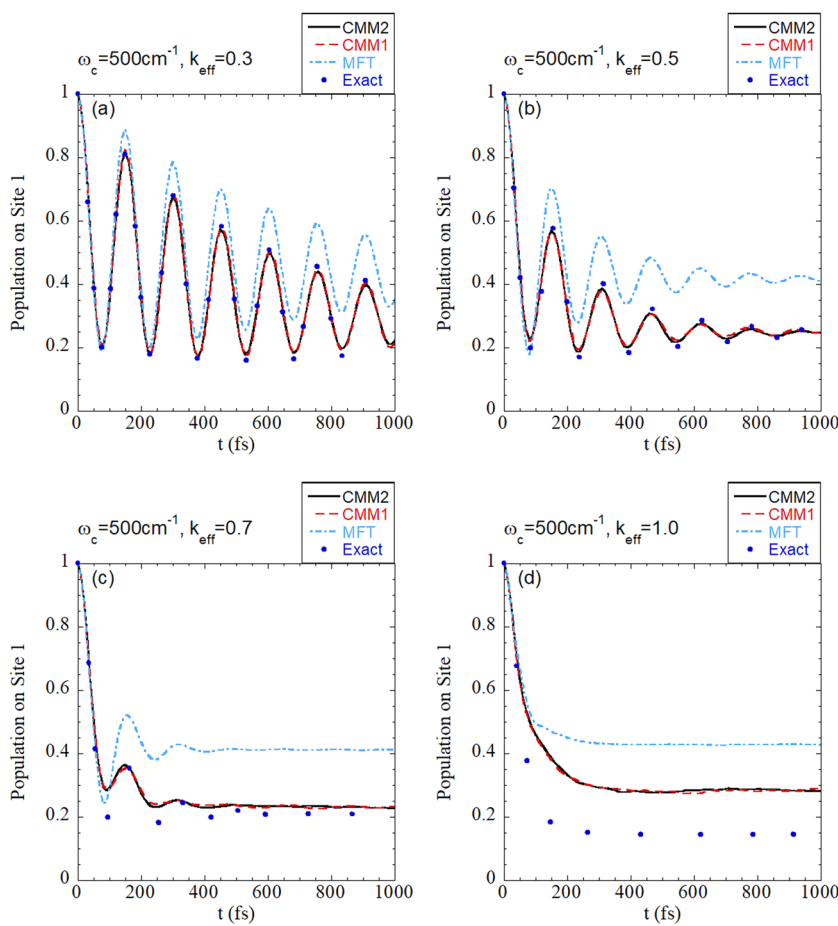

FIG. 24. Same as in Fig. 21, but for ω_c = 500 cm^{-1}. Exact data (produced by MCTDH) are taken from Ref. 83.

As shown in Fig. 21 for the adiabatic region ($\omega_c/V_{12} = 0.4$), CMMs lead to accurate results while MTF shows more notable deviation from exact data as the time is longer and/or as the electron-phonon coupling becomes stronger. Figure 22 illustrates the case on the boundary of the adiabatic and nonadiabatic regions ($\omega_c/V_{12} = 1$). In comparison to the exact results, CMMs demonstrate excellent numerical performance even in the asymptotic region of long time dynamics, but MTF performs progressively worse as the electron-phonon coupling becomes stronger and eventually fails to capture the correct long time asymptote of the population of site 1. Figure 23 depicts the comparison of CMMs to MTF as well as MCTDH in the nonadiabatic region ($\omega_c/V_{12} = 2$). The population of site 1 calculated by CMMs is in overall reasonably good agreement with the numerically exact MCTDH result. MTF demonstrates poor performance even since short time when the electron-phonon coupling is strong. For example, in Fig. 23(d) where the dimensionless parameter for the electron-phonon coupling is $k_{eff} = 1$, MTF fails to yield even qualitative results since 100 fs, while CMMs still lead to a faithful description of the dynamics behaviors even in the asymptotic long time limit. Finally, Fig. 24 presents a challenging model test for condensed phase systems in the nonadiabatic region ($\omega_c/V_{12} = 5$) as ~7% phonon modes (i.e., vibrational modes) of which the frequencies are above 4000 cm^{-1}. This is rare in realistic molecular systems in the condensed phase. Even the high frequency part of the O–H stretching band in liquid water is below 4000 cm^{-1}, as demonstrated in experimental vibrational spectra at room temperature. CMMs capture most dynamics behaviors even in the long-time limit when the electron-phonon coupling is relatively weak ($k_{eff} = 0.3$ or 0.5), yield semiquantitative results even for the long time asymptote of the population of site 1 when $k_{eff} = 0.7$ is employed, and eventually fail to produce the correct asymptotic limit of long time dynamics despite a faithful description of short time dynamics in the strong coupling regime ($k_{eff} = 1.0$). CMMs significantly outperform MFT in all regimes for the asymmetric site-exciton model.

IV. CONCLUSIONS

In this paper, we propose a novel perspective for developing nonadiabatic dynamics approaches based on classical mapping Hamiltonian models in the Cartesian phase space developed in the unified framework.[79] It neither includes any adjustable parameters [such as γ_{nm} in Eq. (7) for accounting for the zero-point energy or quantum commutation for the underlying electronic DOFs] in the mapping Hamiltonian of both electronic and nuclear DOFs [e.g., Eq. (24) for the classical Li-Miller Hamiltonian or Eq. (35) for the classical Meyer-Miller Hamiltonian] nor invokes any SEO states to construct the mapping Hamiltonian or initial conditions. Without these two critical elements used in nearly all applications of the original Meyer-Miller mapping model,[39,42,48,51,53–59,62] classical phase space mapping models are useful to develop nonadiabatic dynamics approaches beyond the MFT (Ehrenfest dynamics) method. The trace over the electronic DOFs is replaced by the physical requirements that the total population is 1 and that the population of each state has to be non-negative and not larger than 1. Various benchmark numerical tests of spin-boson models and of site-exciton models suggest that CMMs can faithfully capture most dynamics behaviors in the short time region as well as in the asymptotic long time region.

It is easy to show that CMMs do *not* encounter the inverted potential energy surface problem during the evolution of the trajectory because Hamilton's equations of motion generated in CMMs guarantee that the population term of each electronic state in the classical mapping Hamiltonian is non-negative. For instance, once the initial condition is chosen from Eq. (28), $x^{(n)}p_y^{(n)} - y^{(n)}p_x^{(n)} = P_n$ is always no less than 0 for any state n in the classical Li-Miller Hamiltonian of Eq. (23) in CMM1 or $\frac{1}{2}\left[\left(x^{(n)}\right)^2 + \left(p^{(n)}\right)^2\right] = P_n$ is guaranteed to be non-negative in the classical Meyer-Miller Hamiltonian of Eq. (35) in CMM2. (Because $\sum_{n=1}^{F} P_n = 1$ is a constant of motion, one obtains $0 \leq P_n \leq 1$ for any state n.) This can be generalized to any other CMMs developed in the unified framework and can be useful for applications to realistic molecular systems. All CMMs can be equally treated in the same simple fashion.

In addition to the LSC-IVR[40,84,85,124–127] for dealing with the dynamics of the nuclear DOFs, other nuclear quantum dynamics methods (such as path integral Liouville dynamics,[128,129] derivative forward-backward semiclassical dynamics,[130–133] other SC-IVR versions,[134–136] ring polymer molecular dynamics,[65–67,72,73,113,137–140] and centroid molecular dynamics[71,141–143]) can also be naturally implemented in the formulation [e.g., Eq. (27) or its other equivalent versions] of CMMs. The new viewpoint in CMMs can also have implication for nonadiabatic dynamics with semiclassical/quasiclassical mapping models in the Cartesian phase space since the pioneering work by Meyer and Miller.[39] It will be interesting in future work to do more investigation for the new viewpoint (for replacing the trace over the electronic DOFs by the constraints for physical requirements) and then develop novel practical nonadiabatic dynamics methods that go beyond conventional MTF,[2–7] surface hopping,[8–24] and mixed quantum-classical dynamics,[28–32] complementing numerically exact approaches (QuAPI,[88–92] MCTDH,[93–98] HEOM,[99–105] and others[144,145]) for studying more general large/complex anharmonic systems (in the condensed phase).

Along with recent progress on the symmetrical quasiclassical (SQC) dynamics with the (triangle) window function technique,[42–53] we expect that the results presented in this paper as well as the unified framework[79] and the isomorphism[80] will encourage more researchers[83,123] to investigate the Meyer-Miller mapping model[39,55,79] as well as other phase space mapping models[79,82] for not only the nonadiabatic dynamics of coupled two- or multi-electronic-state systems but also the nonequilibrium dynamics of the second-quantized many-electron Hamiltonian.[146]

APPENDIX A: FROZEN NUCLEAR CONFIGURATION LIMIT

In the frozen nuclear configuration limit, the time-dependent Schrödinger equation reads

$$i\hbar\dot{\mathbf{c}}(t) = \mathbf{H}\mathbf{c}(t). \tag{A1}$$

Here, $\mathbf{c}(t)$ is a vector for the amplitudes for being in the different electronic states at time t and the Hamiltonian (for a fix nuclear configuration) $\mathbf{H}$ is constant. Define the density matrix $\tilde{\boldsymbol{\rho}}(t) = \mathbf{c}(t)\mathbf{c}^+(t)$, and its time evolution is given by

$$\tilde{\boldsymbol{\rho}}(t) = \mathbf{U}(t)\tilde{\boldsymbol{\rho}}(0)\mathbf{U}^+(t), \tag{A2}$$

where $\mathbf{U}(t) = e^{-i\mathbf{H}t/\hbar}$ is the evolution matrix. Define $\tilde{\rho}_{ij}$ the element in row i and column j of $\tilde{\boldsymbol{\rho}}$ and c_k the kth element of $\mathbf{c}$.

In CMMs, the initial condition from the trace in the electronic DOFs is expressed as

$$c_k = \sqrt{N_k}\exp[i\theta_k] \quad (\forall k), \tag{A3}$$

where the phase of each state is sampled from the independent identical uniform distribution between 0 and 2π, i.e.,

$$\theta_k \overset{iid}{\sim} U[0, 2\pi], \tag{A4}$$

while the action is sampled from the uniform distribution on the surface,

$$\sum_{k=1}^{F} N_k = 1 \text{ with } 0 \le N_k \le 1(\forall k). \tag{A5}$$

For simplicity, we use Θ and Σ to denote Eqs. (A4) and (A5), respectively. Assume that the initial occupation is on the ith electronic state. Consider the population transfer from state i to state j,

$$\langle\tilde{\rho}_{jj}(t)\tilde{\rho}_{ii}(0)\rangle_{\Theta,\Sigma} = \left\langle\left(\mathbf{U}(t)\tilde{\boldsymbol{\rho}}(0)\mathbf{U}^+(t)\right)_{jj}\tilde{\rho}_{ii}(0)\right\rangle_{\Theta,\Sigma}. \tag{A6}$$

Note that $\tilde{\rho}_{ii}(0)$ is a scalar and that the initial conditions Θ and Σ are independent of the evolution matrix $\mathbf{U}(t)$. We recast Eq. (A6) into

$$\langle\tilde{\rho}_{jj}(t)\tilde{\rho}_{ii}(0)\rangle_{\Theta,\Sigma} = \left(\mathbf{U}(t)\langle\tilde{\boldsymbol{\rho}}(0)\tilde{\rho}_{ii}(0)\rangle_{\Theta,\Sigma}\mathbf{U}^+(t)\right)_{jj}. \tag{A7}$$

All off-diagonal terms of $\tilde{\boldsymbol{\rho}}(0)\tilde{\rho}_{ii}(0)$ disappear after averaging over the initial sampling of the phase [Eq. (A4)], i.e.,

$$\langle\tilde{\rho}_{jk}(0)\tilde{\rho}_{ii}(0)\rangle_{\Theta} = \left\langle\sqrt{N_jN_k}e^{i(\theta_j-\theta_k)}N_i\right\rangle_{\Theta} = N_jN_i\delta_{jk}. \tag{A8}$$

Only diagonal elements of $\langle\tilde{\boldsymbol{\rho}}(0)\tilde{\rho}_{ii}(0)\rangle_{\Theta,\Sigma}$, the 2nd matrix in the RHS of Eq. (A7), are nonzero. Its jth diagonal element becomes

$$\langle\tilde{\rho}_{jj}(0)\tilde{\rho}_{ii}(0)\rangle_{\Theta,\Sigma} = \langle N_jN_i\rangle_{\Sigma}. \tag{A9}$$

Here, $\langle N_jN_i\rangle_{\Sigma}$ stands for the average value of N_jN_i over the initial condition Eq. (A5).

Define $S(F) = \int_0^1 dN_1\cdots\int_0^1 dN_F\delta\left(\sum_{k=1}^{F}N_k - 1\right)$ and $x_k = \lambda N_k$. It is easy to show

$$\int_0^\lambda dx_1\cdots\int_0^\lambda dx_F\delta\left(\sum_{k=1}^{F}x_k - \lambda\right)$$

$$= \lambda^F\int_0^1 dN_1\cdots\int_0^1 dN_F\delta\left(\lambda\sum_{k=1}^{F}N_k - \lambda\right)$$

$$= \lambda^{F-1}\int_0^1 dN_1\cdots\int_0^1 dN_F\delta\left(\sum_{k=1}^{F}N_k - 1\right)$$

$$= \lambda^{F-1}S(F). \tag{A10}$$

Equation (A10) proves that constraint Σ is a $F-1$ dimensional measure. One can then show

$$\int_0^1 dN_1\cdots\int_0^1 dN_F\delta\left(\sum_{k=1}^{F}N_k - 1\right)$$

$$= \int_0^1 dN_j\left\{\left[\prod_{k\ne j}\int_0^{1-N_j}dN_k\right]\delta\left(\sum_{k\ne j}N_k - (1 - N_j)\right)\right\}$$

$$= \int_0^1 dN_j(1 - N_j)^{F-2}S(F-1). \tag{A11}$$

That is, $\rho_{\Sigma}(N_j)$ the marginal density distribution of $N_j(\forall j)$ subject to the population constraint Eq. (A5) satisfies

$$\rho_{\Sigma}(N_j) \propto (1 - N_j)^{F-2}. \tag{A12}$$

Equation (A12) leads to

$$\langle N_i\rangle_{\Sigma} = \frac{\int_0^1 N_i\rho_{\Sigma}(N_i)dN_i}{\int_0^1 \rho_{\Sigma}(N_i)dN_i} = \frac{1}{F} \tag{A13}$$

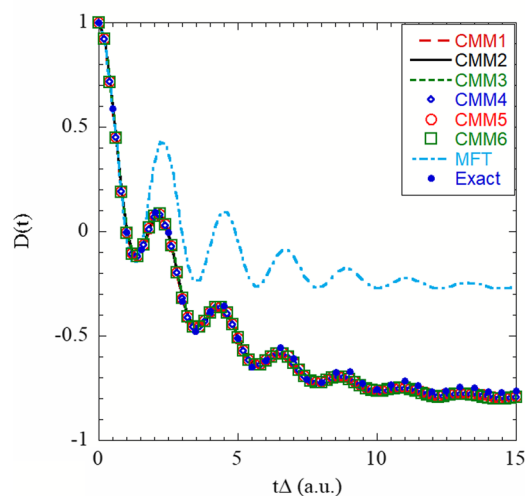Spin-Boson Model 11 for CMM1-6

FIG. 25. Same as in Fig. 11. Red long-dashed line, black solid line, green short-dashed line, blue hollow diamonds, red hollow circles, and green hollow squares illustrate results of CMM1-CMM6 (see Appendix B). For comparison, light blue dotted-dashed line depicts results of MFT, while dark blue solid circles show exact results (produced by QuAPI in Ref. 86).

and

$$\langle N_i^2 \rangle_\Sigma = \frac{\int_0^1 N_i^2 \rho_\Sigma(N_i) dN_i}{\int_0^1 \rho_\Sigma(N_i) dN_i} = \frac{2}{F(F+1)}. \quad \text{(A14)}$$

Substituting Eqs. (A13) and (A14) into the equality

$$\langle N_i^2 \rangle_\Sigma = \left\langle N_i \left(1 - \sum_{j \neq i}^F N_j \right) \right\rangle_\Sigma = \langle N_i \rangle_\Sigma - (F-1)\langle N_j N_i \rangle_{\Sigma, j \neq i} \quad \text{(A15)}$$

yields

$$\langle N_j N_i \rangle_{\Sigma, j \neq i} = \frac{1}{F(F+1)}. \quad \text{(A16)}$$

Equations (A8), (A9), (A14), and (A16) lead to

$$\langle \tilde{\rho}(0)\tilde{\rho}_{ii}(0) \rangle_{\Theta, \Sigma} = \frac{1}{F(F+1)} \mathbf{P}^{(i)}(0) + \frac{1}{F(F+1)} \mathbf{I}. \quad \text{(A17)}$$

Here, $\mathbf{I}$ is an identity matrix that is independent of the initial state i. $\mathbf{P}^{(i)}(0)$ is a matrix whose elements are $P_{jk}^{(i)}(0) = \delta_{ij}\delta_{jk}$. That is, of
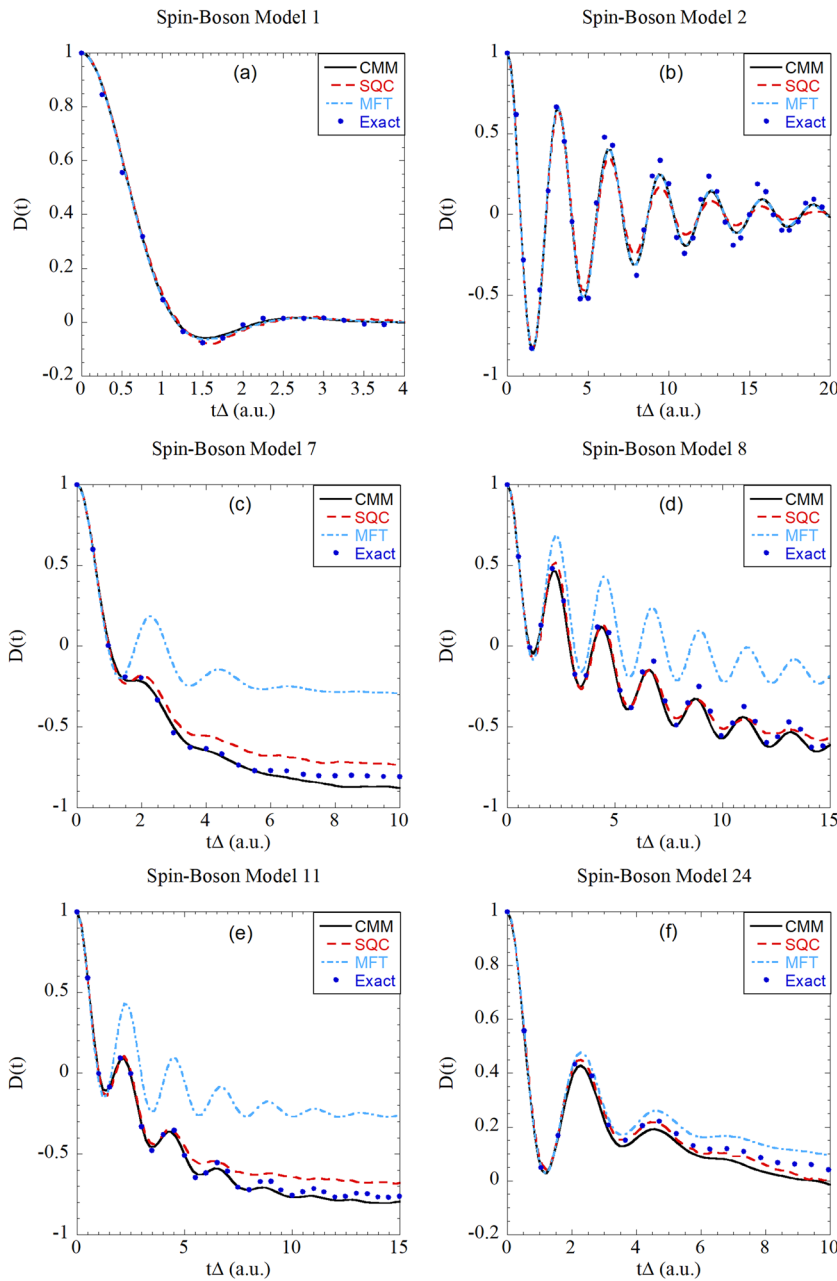

FIG. 26. Comparison of CMM to SQC/MM for six spin-boson models with the Ohmic bath, which are models 1–2 (symmetric cases), models 7–8, model 11, and model 24 (asymmetric cases). Parameters of models 1–2, models 7–8, and model 11 are shown in Figs. 1 and 2, Figs. 7 and 8, and Fig. 11. Parameters for model 24 are $\Delta = 1$, $\varepsilon = 1$, $\beta = 0.25$, $\omega_c = 1$, $\alpha = 0.1$, $dt = 0.01$, and $N_b = 50$. The CMM, SQC, MFT, and exact results are shown in black solid line, red dashed line, blue dashed-dotted line, and dark blue solid circles, respectively. Exact results of model 24 produced by MCTDH are taken from Ref. 94.

matrix $\mathbf{P}^{(i)}(0)$ the element in row i and column i is one, while all other elements are zero.

Substituting Eq. (A17) into Eq. (A7) produces

$$\langle \tilde{\rho}_{jj}(t)\tilde{\rho}_{ii}(0)\rangle_{\Theta,\Sigma} = \frac{1}{F(F+1)}\left(\mathbf{U}(t)\mathbf{P}^{(i)}(0)\mathbf{U}^+(t)\right)_{jj} + \frac{1}{F(F+1)}$$
$$= \frac{1}{F(F+1)}\mathbf{P}^{(i)}_{jj}(t) + \frac{1}{F(F+1)}. \quad (A18)$$

Recall

$$\mathbf{P}^{(i)}_{jj}(t) = \langle j|\mathbf{U}(t)\mathbf{P}^{(i)}(0)\mathbf{U}^+(t)|j\rangle$$
$$= \langle j|\mathbf{U}(t)|i\rangle\langle i|\mathbf{U}^+(t)|j\rangle$$
$$= \left|\langle j|e^{-i\hat{\mathbf{H}}t/\hbar}|i\rangle\right|^2$$
$$= P_{j\leftarrow i}(t). \quad (A19)$$

That is, in the frozen nuclear configuration limit, $\mathbf{P}^{(i)}_{jj}(t)$ is simply the exact population transfer from state i (the initial state) to state j (the final state). Substituting Eq. (A19) into Eq. (A18) leads to

$$P_{j\leftarrow i}(t) = F(F+1)\langle\tilde{\rho}_{jj}(t)\tilde{\rho}_{ii}(0)\rangle_{\Theta,\Sigma} - 1. \quad (A20)$$

That is, the formulation [Eq. (A20)] reproduces the results generated by the time-dependent Schrödinger equation for the electronic state DOFs in the frozen nuclear configuration limit. When nuclear equations of motion are considered in CMMs, Eq. (A20) is the formulation for the population transfer in nonadiabatic dynamics. Equation (32) of Sec. II B is another expression for Eq. (A20).

APPENDIX B: OTHER CLASSICAL MAPPING MODELS FOR NONADIABATIC DYNAMICS

In the unified framework of Ref. 79, in addition to the Li-Miller model as well as the Meyer-Miller model, four more mapping models are proposed. In this paper, we focus on classical mapping models. We extend the formulation [Eqs. (24) and (29) for the Li-Miller mapping model] to the other four mapping Hamiltonian models [Eqs. (11)–(14)], which we denote CMM3, CMM4, CMM5, and CMM6, respectively. As demonstrated in Ref. 79, the six mapping models demonstrate different numerical performance and can be viewed as different integrators for the exact time-dependent Schrödinger equation when nuclear DOFs are frozen. Similarly, when the six CMMs are used to study nonadiabatic dynamics, because all these CMMs are treated in the same fashion, it is expected that they should lead to the same results, although the convergence behavior can be different. We use a challenging model—model 11 (a spin-boson model coupled with the Debye bath)—to test all six CMMs. Figure 25 indicates that all six CMMs yield the same converged results. This is also true for all other spin-boson models or site-exciton models presented in this paper.
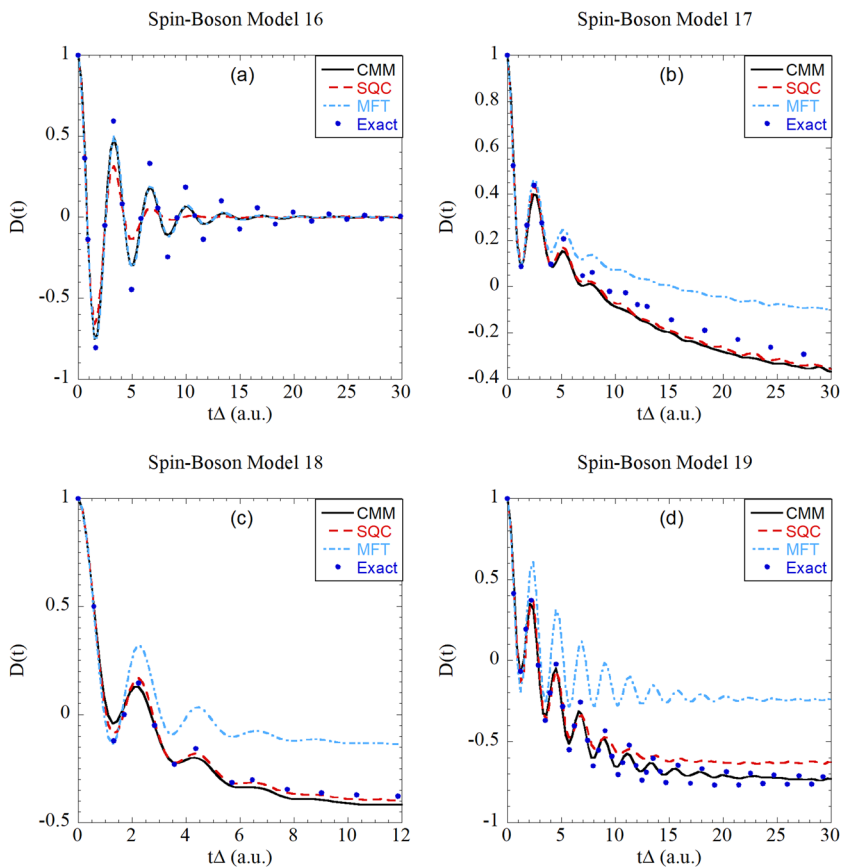
FIG. 27. Comparison of CMM to SQC/MM for four spin-boson models with the Debye bath, which are model 16 (symmetric case) and models 17–19 (asymmetric cases). Parameters are listed in Figs. 16–19. Markers are the same as in Fig. 26.
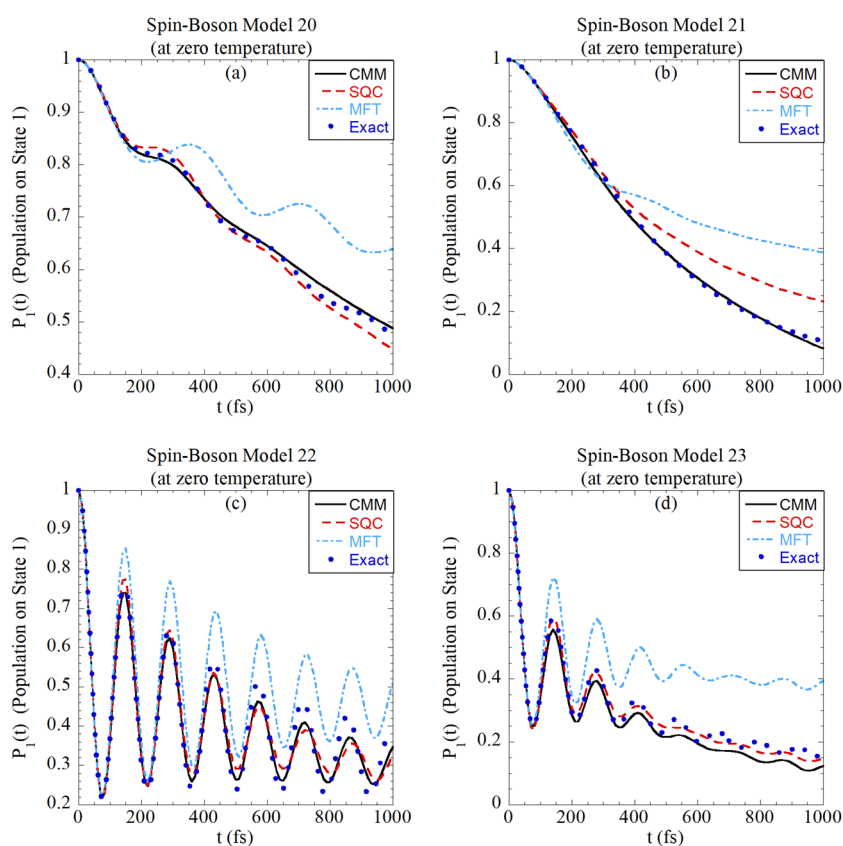
FIG. 28. Comparison of CMM to SQC/MM for four asymmetric spin-boson models with the Ohmic bath at zero temperature (models 20–23). Parameters are listed in Fig. 20. Markers are the same as in Fig. 26.

When the six Hamiltonian models in the phase space are treated semiclassically or quasiclassically, they may show different numerical behaviors if not treated in the same fashion.

APPENDIX C: COMPARISON OF CLASSICAL MAPPING MODELS TO SYMMETRICAL QUASICLASSICAL MEYER-MILLER APPROACH

The symmetrical quasiclassical Meyer-Miller (SQC/MM) approach with the window function technique[42–53] has been demonstrated as a promising nonadiabatic dynamics method. We employ the most recent version of the SQC/MM approach (with the triangle window function)[48,50,52,53] for comparison to CMMs. We investigate six typical spin-boson models with the Ohmic bath (as shown in Fig. 26) and four typical spin-boson models with the Debye bath (as shown in Fig. 27).

When symmetric spin-boson models are studied as shown in Fig. 26(b) (for model 2) and Fig. 27(a) (for model 16), SQC/MM leads to faster decay in comparison to CMMs as well as numerically exact approaches. When asymmetric spin-boson models are considered, SQC/MM demonstrates slightly better performance than CMMs in Fig. 26(f) (for model 24), Fig. 27(c) (for model 18), and Fig. 28(d) (for model 23), while CMMs mildly outperform SQC/MM in Fig. 26(c) (for model 7), Fig. 26(d) (for model 8), Fig. 26(e) (for model 11), Fig. 27(d) (for model 19), Fig. 28(b) (for model 21), and Fig. 28(c) (for model 22). Although different strategies are

employed, CMMs show overall comparable accuracy to SQC/MM. It will be interesting in future work to thoroughly investigate the new strategy proposed in this paper and those strategies used in other nonadiabatic dynamics methods based on phase space mapping models[39–49,51–63,75,76] to formulate a more accurate and practical trajectory-based approach for condensed phase nonadiabatic systems.

REFERENCES

[1]W. Domcke, D. R. Yarkony, and H. Koppel, *Conical Intersections: Theory, Computation and Experiment* (World Scientific, Singapore, 2010).
[2]X. S. Li, J. C. Tully, H. B. Schlegel, and M. J. Frisch, J. Chem. Phys. **123**(8), 084106 (2005).
[3]D. V. Shalashilin, Faraday Discuss. **153**, 105–116 (2011).
[4]D. V. Makhov, C. Symonds, S. Fernandez-Alberti, and D. V. Shalashilin, Chem. Phys. **493**, 200–218 (2017).
[5]X. Andrade, A. Castro, D. Zueco, J. L. Alonso, P. Echenique, F. Falceto, and A. Rubio, J. Chem. Theory Comput. **5**(4), 728–742 (2009).
[6]A. Bastida, C. Cruz, J. Zuniga, A. Requena, and B. Miguel, Chem. Phys. Lett. **417**(1-3), 53–57 (2006).
[7]A. Ojanpera, V. Havu, L. Lehtovaara, and M. Puska, J. Chem. Phys. **136**(14), 144103 (2012).
[8]J. C. Tully, J. Chem. Phys. **93**(2), 1061–1071 (1990).
[9]J. C. Tully, Faraday Discuss. **110**, 407–419 (1998).
[10]J. C. Tully, J. Chem. Phys. **137**(22), 22a301 (2012).
[11]W. Xie and W. Domcke, J. Chem. Phys. **147**(18), 184114 (2017).

[12]A. V. Akimov and O. V. Prezhdo, Chem. Rev. **115**(12), 5797–5890 (2015).

[13]L. Wang, A. Akimov, and O. V. Prezhdo, J. Phys. Chem. Lett. **7**(11), 2100–2112 (2016).

[14]S. Hammes-Schiffer, J. Am. Chem. Soc. **137**(28), 8860–8871 (2015).

[15]E. Brunk and U. Rothlisberger, Chem. Rev. **115**(12), 6217–6263 (2015).

[16]S. Mai, P. Marquetand, and L. Gonzalez, Int. J. Quantum Chem. **115**(18), 1215–1231 (2015).

[17]G. Cui and W. Thiel, J. Chem. Phys. **141**(12), 124101 (2014).

[18]L. Spoerkel and W. Thiel, J. Chem. Phys. **144**(19), 194108 (2016).

[19]J. E. Subotnik, A. Jain, B. Landry, A. Petit, W. Ouyang, and N. Bellonzi, in *Annual Review of Physical Chemistry*, edited by M. A. Johnson and T. J. Martinez (Annual Reviews, 2016), Vol. 67, pp. 387–417.

[20]O. Weingart, Curr. Org. Chem. **21**(7), 586–601 (2017).

[21]F. F. de Carvalho, M. E. F. Bouduban, B. F. E. Curchod, and I. Tavernelli, Entropy **16**(1), 62–85 (2014).

[22]M. Persico and G. Granucci, Theor. Chem. Acc. **133**(9), 1526 (2014).

[23]R. Crespo-Otero and M. Barbatti, Chem. Rev. **118**(15), 7026–7068 (2018).

[24]H.-T. Chen and D. R. Reichman, J. Chem. Phys. **144**(9), 094104 (2016).

[25]N. Makri, Int. J. Quantum Chem. **115**(18), 1209–1214 (2015).

[26]P. L. Walters and N. Makri, J. Phys. Chem. Lett. **6**(24), 4959–4965 (2015).

[27]P. L. Walters and N. Makri, J. Chem. Phys. **144**(4), 044108 (2016).

[28]R. Kapral, Chem. Phys. **481**, 77–83 (2016).

[29]R. Kapral and G. Ciccotti, J. Chem. Phys. **110**(18), 8919–8929 (1999).

[30]A. Kelly, R. van Zon, J. Schofield, and R. Kapral, J. Chem. Phys. **136**(8), 084101 (2012).

[31]Q. Shi and E. Geva, J. Chem. Phys. **131**(3), 034511 (2009).

[32]W. Xie, M. Xu, S. Bai, and Q. Shi, J. Phys. Chem. A **120**(19), 3225–3232 (2016).

[33]D. V. Makhov, T. J. Martinez, and D. V. Shalashilin, Faraday Discuss. **194**, 81–94 (2016).

[34]M. Ben-Nun, J. Quenneville, and T. J. Martinez, J. Phys. Chem. A **104**(22), 5161–5175 (2000).

[35]M. Ben-Nun and T. J. Martinez, Adv. Chem. Phys. **121**, 439–512 (2002).

[36]B. G. Levine, J. D. Coe, A. M. Virshup, and T. J. Martinez, Chem. Phys. **347**(1-3), 3–16 (2008).

[37]B. F. E. Curchod and T. J. Martinez, Chem. Rev. **118**(7), 3305–3336 (2018).

[38]D. V. Makhov, W. J. Glover, T. J. Martinez, and D. V. Shalashilin, J. Chem. Phys. **141**(5), 054110 (2014).

[39]H.-D. Meyer and W. H. Miller, J. Chem. Phys. **70**, 3214–3223 (1979).

[40]X. Sun, H. B. Wang, and W. H. Miller, J. Chem. Phys. **109**(17), 7064–7074 (1998).

[41]E. A. Coronado, V. S. Batista, and W. H. Miller, J. Chem. Phys. **112**(13), 5566–5575 (2000).

[42]S. J. Cotton and W. H. Miller, J. Chem. Phys. **139**(23), 234112 (2013).

[43]S. J. Cotton and W. H. Miller, J. Phys. Chem. A **117**(32), 7190–7194 (2013).

[44]S. J. Cotton, K. Igumenshchev, and W. H. Miller, J. Chem. Phys. **141**(8), 084104 (2014).

[45]S. J. Cotton and W. H. Miller, J. Phys. Chem. A **119**(50), 12138–12145 (2015).

[46]W. H. Miller and S. J. Cotton, J. Chem. Phys. **142**(13), 131103 (2015).

[47]W. H. Miller and S. J. Cotton, J. Chem. Phys. **145**(8), 081102 (2016).

[48]S. J. Cotton and W. H. Miller, J. Chem. Phys. **145**(14), 144108 (2016).

[49]S. J. Cotton and W. H. Miller, J. Chem. Theory Comput. **12**(3), 983–991 (2016).

[50]W. H. Miller and S. J. Cotton, Faraday Discuss. **195**, 9–30 (2016).

[51]S. J. Cotton, R. Liang, and W. H. Miller, J. Chem. Phys. **147**(6), 064112 (2017).

[52]R. B. Liang, S. J. Cotton, R. Binder, R. Hegger, I. Burghardt, and W. H. Miller, J. Chem. Phys. **149**(4), 044101 (2018).

[53]S. J. Cotton and W. H. Miller, J. Chem. Phys. **150**(10), 104101 (2019).

[54]A. A. Kananenka, C.-Y. Hsieh, J. Cao, and E. Geva, J. Phys. Chem. Lett. **9**(2), 319–326 (2018).

[55]G. Stock and M. Thoss, Phys. Rev. Lett. **78**(4), 578–581 (1997).

[56]U. Muller and G. Stock, J. Chem. Phys. **111**(1), 77–88 (1999).

[57]M. Thoss and G. Stock, Phys. Rev. A **59**(1), 64–79 (1999).

[58]G. Stock and M. Thoss, in *Advances in Chemical Physics*, edited by S. A. Rice (John Wiley & Sons, Inc., 2005), Vol. 131, pp. 243–375.

[59]A. A. Golosov and D. R. Reichman, J. Chem. Phys. **114**(3), 1065–1074 (2001).

[60]S. Bonella and D. F. Coker, J. Chem. Phys. **122**(19), 194102 (2005).

[61]G. Tao, J. Chem. Phys. **144**(9), 094108 (2016).

[62]M. A. C. Saller, A. Kelly, and J. O. Richardson, J. Chem. Phys. **150**(7), 071101 (2019).

[63]P. Huo and D. F. Coker, J. Chem. Phys. **135**(20), 201101 (2011).

[64]P. Shushkov, R. Li, and J. C. Tully, J. Chem. Phys. **137**(22), 22a549 (2012).

[65]J. O. Richardson and M. Thoss, J. Chem. Phys. **139**(3), 031102 (2013).

[66]N. Ananth, J. Chem. Phys. **139**(12), 124102 (2013).

[67]S. N. Chowdhury and P. Huo, J. Chem. Phys. **147**(21), 214109 (2017).

[68]X. Tao, P. Shushkov, and T. F. Miller III, J. Chem. Phys. **148**(10), 102327 (2018).

[69]A. Abedi, F. Agostini, and E. K. U. Gross, Europhys. Lett. **106**(3), 33001 (2014).

[70]S. K. Min, F. Agostini, I. Tayernelli, and E. K. U. Gross, J. Phys. Chem. Lett. **8**(13), 3048–3055 (2017).

[71]J. L. Liao and G. A. Voth, J. Phys. Chem. B **106**(33), 8449–8455 (2002).

[72]A. R. Menzeleev, F. Bell, and T. F. Miller III, J. Chem. Phys. **140**(6), 064103 (2014).

[73]J. R Duke and N. Ananth, Faraday Discuss. **195**, 253–268 (2016).

[74]N. Ananth and T. F. Miller III, J. Chem. Phys. **133**(23), 234103 (2010).

[75]P. F. Huo and D. F. Coker, J. Chem. Phys. **137**(22), 22A535 (2012).

[76]P. F. Huo, T. F. Miller, and D. F. Coker, J. Chem. Phys. **139**(15), 151103 (2013).

[77]J. Schwinger, in *Quantum Theory of Angular Momentum*, edited by L. C. Biedenharn and H. VanDam (Academic, New York, 1965).

[78]J. J. Sakurai, *Modern Quantum Mechanics* (Addison-Wesley, New York, 1994).

[79]J. Liu, J. Chem. Phys. **145**(20), 204105 (2016).

[80]J. Liu, J. Chem. Phys. **146**(2), 024110 (2017).

[81]G. Stock and U. Muller, J. Chem. Phys. **111**(1), 65–76 (1999).

[82]B. Li and W. H. Miller, J. Chem. Phys. **137**(15), 154107 (2012).

[83]J. Zheng, Y. Xie, S.-s. Jiang, Y.-z. Long, X. Ning, and Z. Lan, e-print arXiv:1811.00257 [physics.chem-ph] (2018).

[84]H. Wang, X. Sun, and W. H. Miller, J. Chem. Phys. **108**(23), 9726–9736 (1998).

[85]J. Liu and W. H. Miller, J. Chem. Phys. **131**(7), 074113 (2009).

[86]A. Kelly, A. Montoya-Castillo, L. Wang, and T. E. Markland, J. Chem. Phys. **144**(18), 184105 (2016).

[87]A. J. Leggett, S. Chakravarty, A. T. Dorsey, M. P. A. Fisher, A. Garg, and M. Zwerger, Rev. Mod. Phys. **59**, 1–85 (1987).

[88]D. E. Makarov and N. Makri, Chem. Phys. Lett. **221**(5-6), 482–491 (1994).

[89]N. Makri and D. E. Makarov, J. Chem. Phys. **102**(11), 4600–4610 (1995).

[90]N. Makri and D. E. Makarov, J. Chem. Phys. **102**(11), 4611–4618 (1995).

[91]M. Topaler and N. Makri, J. Phys. Chem. **100**(11), 4430–4436 (1996).

[92]F. Nesi, E. Paladino, M. Thorwart, and M. Grifoni, Europhys. Lett. **80**(4), 40005 (2007).

[93]M. Thoss, H. B. Wang, and W. H. Miller, J. Chem. Phys. **115**(7), 2991–3005 (2001).

[94]H. B. Wang, M. Thoss, and W. H. Miller, J. Chem. Phys. **115**(7), 2979–2990 (2001).

[95]G. A. Worth, H. D. Meyer, H. Koeppel, L. S. Cederbaum, and I. Burghardt, Int. Rev. Phys. Chem. **27**(3), 569–606 (2008).

[96]H. B. Wang and M. Thoss, J. Chem. Phys. **119**(3), 1289–1299 (2003).

[97]H. B. Wang and M. Thoss, New J. Phys. **10**, 115005 (2008).

[98]H. B. Wang and M. Thoss, Chem. Phys. **370**(1-3), 78–86 (2010).

[99]Y. A. Yan, F. Yang, Y. Liu, and J. S. Shao, Chem. Phys. Lett. **395**(4-6), 216–221 (2004).

[100]Y. Zhou and J. Shao, J. Chem. Phys. **128**(3), 034106 (2008).

[101]J. Hu, M. Luo, F. Jiang, R. X. Xu, and Y. J. Yan, J. Chem. Phys. **134**(24), 244106 (2011).

[102]H. Liu, L. L. Zhu, S. M. Bai, and Q. Shi, J. Chem. Phys. **140**(13), 134106 (2014).

[103]Y. Tanimura, J. Chem. Phys. **141**(4), 044114 (2014).

[104]Z. Tang, X. Ouyang, Z. Gong, H. Wang, and J. Wu, J. Chem. Phys. **143**(22), 224112 (2015).

[105]M. Xu, Y. M. Yan, Y. Y. Liu, and Q. Shi, J. Chem. Phys. **148**(16), 164101 (2018).

[106]X. Liu and J. Liu, J. Chem. Phys. **148**(10), 102319 (2017).

[107]H. Wang, X. Liu, and J. Liu, Chin. J. Chem. Phys. **31**(4), 446–456 (2018).

[108]A. Garg, J. N. Onuchic, and V. Ambegaokar, J. Chem. Phys. **83**(9), 4491–4503 (1985).

[109]H. B. Wang, X. Y. Song, D. Chandler, and W. H. Miller, J. Chem. Phys. **110**(10), 4828–4840 (1999).

[110]A. Ishizaki and G. R. Fleming, Proc. Natl. Acad. Sci. U. S. A. **106**(41), 17255–17260 (2009).

[111]M. Topaler and N. Makri, J. Chem. Phys. **101**(9), 7500–7519 (1994).

[112]N. Makri, J. Chem. Phys. **111**(14), 6164–6167 (1999).

[113]I. R. Craig and D. E. Manolopoulos, J. Chem. Phys. **122**(8), 084106 (2005).

[114]I. R. Craig, M. Thoss, and H. Wang, J. Chem. Phys. **127**(14), 144503 (2007).

[115]H. Wang, J. Phys. Chem. A **118**(39), 9253–9261 (2014).

[116]A. Kelly, N. Brackbill, and T. E. Markland, J. Chem. Phys. **142**(9), 094110 (2015).

[117]Q. L. Wang, Z. H. Gong, C. R. Duan, Z. F. Tang, and J. L. Wu, J. Chem. Phys. **150**(8), 084114 (2019).

[118]R. Bulla, N. H. Tong, and M. Vojta, Phys. Rev. Lett. **91**(17), 170601 (2003).

[119]A. Ishizaki and G. R. Fleming, J. Chem. Phys. **130**(23), 234111 (2009).

[120]A. Ishizaki and G. R. Fleming, J. Chem. Phys. **130**(23), 234110 (2009).

[121]H. Tamura, I. Burghardt, and M. Tsukada, J. Phys. Chem. C **115**(20), 10205–10210 (2011).

[122]Y. Xie, J. Zheng, and Z. G. Lan, J. Chem. Phys. **142**(8), 084706 (2015).

[123]Y. Xie, J. Zheng, and Z. Lan, J. Chem. Phys. **149**(17), 174105 (2018).

[124]Q. Shi and E. Geva, J. Chem. Phys. **118**(18), 8173 (2003).

[125]J. A. Poulsen, G. Nyman, and P. J. Rossky, J. Chem. Phys. **119**(23), 12179 (2003).

[126]J. S. Shao, J. L. Liao, and E. Pollak, J. Chem. Phys. **108**(23), 9711–9725 (1998).

[127]J. Liu, Int. J. Quantum Chem. **115**(11), 657–670 (2015).

[128]J. Liu, J. Chem. Phys. **140**(22), 224107 (2014).

[129]J. Liu and Z. Zhang, J. Chem. Phys. **144**(3), 034307 (2016).

[130]J. Liu, A. Nakayama, and N. Makri, Mol. Phys. **104**(8), 1267–1274 (2006).

[131]N. Makri, A. Nakayama, and N. Wright, J. Theor. Comput. Chem. **3**, 391–417 (2004).

[132]J. Shao and N. Makri, J. Phys. Chem. A **103**, 7753–7756 (1999).

[133]J. Shao and N. Makri, J. Phys. Chem. A **103**, 9479–9486 (1999).

[134]W. H. Miller, J. Phys. Chem. A **105**(13), 2942–2955 (2001).

[135]W. H. Miller, Proc. Natl. Acad. Sci. U. S. A. **102**(19), 6660–6664 (2005).

[136]W. H. Miller, J. Chem. Phys. **125**(13), 132305 (2006).

[137]J. O. Richardson and S. C. Althorpe, J. Chem. Phys. **131**(21), 214106 (2009).

[138]S. Habershon, D. E. Manolopoulos, T. E. Markland, and T. F. Miller III, Annu. Rev. Phys. Chem. **64**, 387–413 (2013).

[139]M. Rossi, M. Ceriotti, and D. E. Manolopoulos, J. Chem. Phys. **140**(23), 234116 (2014).

[140]J. R. Duke and N. Ananth, J. Phys. Chem. Lett. **6**(21), 4219–4223 (2015).

[141]J. Cao and G. A. Voth, J. Chem. Phys. **99**(12), 10070–10073 (1993).

[142]T. D. Hone, P. J. Rossky, and G. A. Voth, J. Chem. Phys. **124**(15), 154103 (2006).

[143]G. A. Voth, Adv. Chem. Phys. **93**, 135 (1996).

[144]S. M. Greene and V. S. Batista, J. Chem. Theory Comput. **13**(9), 4034–4042 (2017).

[145]M. D. Hack, A. M. Wensmann, D. G. Truhlar, M. Ben-Nun, and T. J. Martinez, J. Chem. Phys. **115**(3), 1172–1186 (2001).

[146]B. Li, E. Y. Wilner, M. Thoss, E. Rabani, and W. H. Miller, J. Chem. Phys. **140**(10), 104110 (2014).